

Non-parametric Kernel-Based Estimation of Probability Distributions for Precipitation Modeling

Andrew Pavlides^a, Vasiliki Agou^a, Dionissios T. Hristopoulos^{b,*}

^a*School of Mineral Resources Engineering, Technical University of Crete, Chania, Crete 73100, Greece*

^b*School of Electrical and Computer Engineering, Technical University of Crete, Chania, Crete 73100, Greece*

Abstract

The probability distribution of precipitation amount strongly depends on geography, climate zone, and time scale considered. Closed-form parametric probability distributions are not sufficiently flexible to provide accurate and universal models for precipitation amount over different time scales. In this paper we derive non-parametric estimates of the cumulative distribution function (CDF) of precipitation amount for wet time intervals. The CDF estimates are obtained by integrating the kernel density estimator leading to semi-explicit CDF expressions for different kernel functions. We investigate kernel-based CDF estimation with an adaptive plug-in bandwidth (KCDE), using both synthetic data sets and reanalysis precipitation data from the island of Crete (Greece). We show that KCDE provides better estimates of the probability distribution than the standard empirical (staircase) estimate and kernel-based estimates that use the normal reference bandwidth. We also demonstrate that KCDE enables the simulation of non-parametric precipitation amount distributions by means of the inverse transform sampling method.

Keywords: precipitation, kernel density estimation, simulation, non-Gaussian, reanalysis data, non-parametric estimate

*Corresponding author

Email addresses: dchristopoulos@ece.tuc.gr (Dionissios T. Hristopoulos),
dchristopoulos@ece.tuc.gr (Dionissios T. Hristopoulos)

URL: <http://www.geostatistics.tuc.gr/4908.html> (Dionissios T. Hristopoulos)

1. Introduction

Precipitation is a key component of the hydrologic cycle. It is particularly important for the health of ecosystems and the well-being of human societies, since it helps to recharge aquifers and surface water bodies thus contributing to economic activity and the preservation of biodiversity. On the other hand, modeling precipitation is not an easy task. Features such as the intensity and duration of precipitation vary significantly depending on geographic location, climate zone, season, and local topography. There are also strong interannual variations in the amount of precipitation over any given geographical area.

Since precipitation is an inherently stochastic process, its properties are modeled by means of probability distributions. Reflecting the highly variable features of precipitation, such probability distributions vary significantly depending on the location and the time scales of the measurements, as well as the modalities by means of which the data are obtained (e.g., rain gauges, satellite sensors, radar-based estimates, reanalysis methods).

To further complicate the situation, climate change has an impact on the precipitation patterns globally. It affects the duration and rate of precipitation events, the return periods, and the total amount of precipitation received by an area. This is a major cause of concern, since altered precipitation patterns can destabilize ecosystems, cause significant economic damage due to extreme events, and ruin local economies. The risk is greater in certain vulnerable areas of the globe which include the Mediterranean basin. Precipitation plays a crucial role in the life of the major Mediterranean islands (e.g., Sicily, Sardinia, Cyprus, Corsica, and Crete). Changes in the intensity and total amount of precipitation, in combination with increased demand for water due to tourism and agricultural activities, can lead to soil erosion, depletion of groundwater aquifers, extinction of flora and fauna, increased flooding, salt water intrusion into aquifers, and eventually desertification. Hence, monitoring precipitation, as well as other water resources, and developing accurate quantitative models and decision making tools are important steps towards predicting the impacts of climate change and proposing effective policies to mitigate them.

The intensity (rain rate) and total amount of precipitation over a specified aggregation time window are often modeled using parametric approaches. Time windows of one hour, one day during the wet period, an entire month, an entire season, or one year are used. Common parametric models include the exponential, mixed exponential, gamma, lognormal, generalized gamma,

Weibull, generalized extreme value (GEV), as well as hybrid mixtures of exponential with a Pareto tail [1, 2].

The gamma distribution is a popular choice, regardless of the observation time window over which data are aggregated [2]. It has been used to model daily rain rates [3], as well as monthly and seasonal precipitation anomalies [4, 5]. It adequately models the variation of precipitation amounts in wet periods with a scale parameter proportional to the number of days and a shape parameter independent of the length of the observation window [6]. Zero precipitation values are taken into account in the gamma model using Type I censoring of the distribution on the left [4]. Left censoring implies that the number of values below a given threshold is considered known, but the exact values are not. The same approach can also be used for the other distributions discussed below.

The lognormal distribution has been used to approximate rain-rate [7, 8, 9], cumulus cloud populations [10], hourly precipitation [11], storm height distribution over the tropical oceans [12], amount of precipitable water [13, 14], and the estimated average rain rate from satellite observations [15]. A recent study of the lognormal and gamma distributions concluded that both fit satisfactorily TRMM data (obtained from the Tropical Rainfall Measuring Mission research satellite which operated from 1997 to 2015) of daily average rain-rate [3].

The Generalized Extreme Value (GEV) distribution has been applied to modeling of precipitation amount and extremes over different time scales, such as maximum one-day rainfall [16, 17], k -day extreme precipitation (for k ranging between 1 and 30) [18], daily precipitation forecasts [19], annual maximum precipitation [20], monthly return levels and their annual cycle [21], and seasonal extremes using ensembles of climate models [22]. Hybrid GEV models that allow more flexible tail behavior are considered in [23, 24].

Parametric models offer the advantage of closed-form expressions for the probability density function, and in most cases for all the main probability functions (i.e., cumulative distribution, survival, and hazard rate functions). In addition, they are motivated by theoretical arguments. For example, the Fisher–Tippett–Gnedenko theorem states that the maximum of a sample of independent, identically distributed random variables (after suitable affine transformation) converges in distribution to the GEV family (which includes the Gumbel, Fréchet, and Weibull models) [25, 26]. A recent analysis based on stochastic modeling of the competing factors in the atmospheric moisture budget justifies the use of the gamma distribution for precipitation inten-

sity [27].

In spite of their considerable advantages, parametric models have a number of shortcomings. One of them is their limited flexibility. For example, a recent study of daily precipitation values over Europe showed that the gamma distribution is not supported by rigorous statistical testing at more than 40% of the examined stations [28]. In certain cases, a parametric expression of the cumulative distribution function (CDF) cannot be easily deduced. Such an example is the amount of monthly precipitation in semi-arid Mediterranean areas [29].

Standard parametric probability models (e.g., exponential, gamma distribution) may also fail to capture both the low-value (left tail) and high-value (right tail) regimes of the data distribution. This has motivated the introduction of hybrid models, which combine more than one distribution types. Another problem is that the parametric models assume stationarity, i.e., that the parameters of the distribution remain constant during the time of observation. However, in light of the accelerating effects of climate change on meteorological variables such as temperature and precipitation [30], it is difficult to justify the stationarity assumption [31]. Moreover, parametric models that have proved satisfactory in the past may not adequately capture precipitation patterns in future climate. This concern is fueled by the expected increase of extreme precipitation events [31], as well as climate model simulations predicting changes in the statistical patterns of daily precipitation extremes [32].

Non-parametric approaches that estimate the probability distribution from the data without reference to a specific mathematical form provide a useful alternative to parametric models. The simplest non-parametric estimator is the empirical CDF, which has the form of a non-decreasing step function (a staircase). However, the empirical CDF is discontinuous. This is unsatisfactory for continuously-valued variables such as the rain rate, especially for limited sample size. In addition, the staircase estimate is not suitable for the simulation of continuous variables.

Non-parametric kernel density (KDE) estimation (known as the Parzen Rosenblatt window method) allows constructing approximations of the probability density function (PDF) without step discontinuities [33, 34]. Kernel density estimators employ a bandwidth parameter h which determines the range of the kernel function and controls the smoothness of the estimated PDF [35].

Selection of an optimal KDE bandwidth for the available data is an im-

portant problem in statistics [36, 37, 38]. Various theoretical and empirical approaches have been proposed for bandwidth selection. Plug-in methods are based on *a priori* assumptions about the probability distribution of the data. They are derived by minimizing the Asymptotic Mean Integrated Square Error between the KDE and the unknown PDF [39, 37, 38, 35]. For example, if the data follow the normal probability distribution $\mathcal{N}(m, \sigma^2)$, the *normal reference rule (rule of thumb)* gives the optimal bandwidth h for the Gaussian kernel as $h = 1.06\sigma N^{-1/5}$, where N is the data size [40].

Non-parametric approaches have been proposed for the study of precipitation. For instance, [41, 42] reported on KDE and its application in the simulation of daily precipitation. The study [43] reports on non-parametric precipitation distribution modeling using the Gaussian kernel and numerical integration of the density. The normal reference rule bandwidth with the interquartile range as measure of scale [40] and the Sheather-Jones plug-in bandwidth [39] were tested and returned comparable results.

We propose a non-parametric, kernel-based estimator (KCDE) which targets the CDF instead of the PDF. We analytically evaluate the kernel integrals which form the KCDE building blocks for selected kernel functions with both compact and infinite support. Based on synthetic data sets, we show that KCDE equipped with the plug-in BGK bandwidth derived by Botev, Grotowski, and Kroese [44] estimates the data probability distribution more accurately than the normal reference bandwidth which is typically used in KDE. In addition, KCDE allows the efficient simulation of precipitation amounts from the non-parametric CDF by means of the inverse transform sampling method. We test KCDE performance against the empirical CDFs for several kernel functions.

Our analysis employs synthetic precipitation data motivated by rain gauge measurements as well as ERA5 reanalysis products for the Mediterranean island of Crete (Greece). Crete is a major Mediterranean island (fifth in size overall and the largest island of Greece), where the combination of adverse climate change forecasts, and increasing tourist and agricultural activities poses serious threats to the sustainability of the island’s water resources [45, 46, 47].

The remainder of this paper is structured as follows: Section 2 describes the methods used. First, it provides a short synopsis of the investigated probability distribution models. This is followed by an overview of the estimation of kernel-based PDF, $\hat{f}_k(z)$ functions. Then, the integrals involved in kernel-based CDFs, $\hat{F}_k(z)$, are evaluated for selected kernel functions (the calculations are shown in detail in Appendix A). Last, the BGK plug-in

bandwidth estimation by [44] is reviewed (details of the algorithm are given in Appendix B). Applications of KCDE using the BGK bandwidth to synthetic data are investigated in Section 3. The parameters of these distributions are motivated by the statistical features of monthly rainfall amount data for the island of Crete [29]. Additional results comparing KCDE with the normal reference bandwidth are given in Appendix C. Section 4 applies KCDE to ERA5 reanalysis precipitation data. Section 5 focuses on the simulation of precipitation amounts based on the KCDE-derived $\hat{F}_k(z)$ and the inverse transform sampling (ITS) method. Discussion, conclusions and suggestions for further studies are given in Section 6.

2. Methodology

In the following, we assume that the precipitation rate is a continuous-time, stationary stochastic process $R(t; \omega)$ defined over a probability space (Ω, \mathcal{F}, P) , where $\omega \in \Omega$ is the state index in the sample space Ω , \mathcal{F} is a σ -algebra of events, and P is the probability measure for these events [48, 49].

The data comprise precipitation amounts (z_1, z_2, \dots, z_N) observed at times t_1, t_2, \dots, t_N . The times $t_n = n\delta t$ are multiples of a characteristic time step δt , corresponding to one day, week, month, season, or year. The amounts z_n represent the cumulative amount of precipitation over the time interval $[t_{n-1}, t_n)$. We focus on wet time intervals, i.e., $z_n > 0$ for all n . The cumulative precipitation represents samples of the following stochastic integral (for definition see [48]):

$$Z_{\delta t}(t_n; \omega) = \int_{t_{n-1}}^{t_n} dt R(t; \omega), \quad n = 1, \dots, N.$$

In the following, for brevity we refer to $Z_{\delta t}(t_n; \omega)$ as $Z(t; \omega)$. However, $Z(t; \omega)$ implicitly depends on the averaging window δt . Multiple samples from the same probability model will be distinguished by means of the index $m = 1, \dots, M$, i.e., $Z_N^{(m)} = (z_1^{(m)}, z_2^{(m)}, \dots, z_N^{(m)})^\top$, where \top denotes the transpose of a matrix or vector. Different models will be distinguished by means of the integer subscript j , i.e., $Z_{N;j}^{(m)}$, $j = 1, \dots, J$ and J is the number of models tested. The marginal CDF of $Z(t; \omega)$ is defined by $F(z) = \text{Prob}(Z \leq z)$ and the marginal PDF by $f(z) = \frac{dF(z)}{dz}$. The respective estimates of the CDF and PDF from the data are denoted by $\hat{F}_K(z)$,

$\hat{f}_K(z)$ if the estimates are based on KDE and $\hat{F}_s(z)$, $\hat{f}_s(z)$ if the estimates are obtained by means of the empirical staircase function.

A smoothing kernel is a real-valued, non-negative function $K(z - z'; h) = K(\frac{z-z'}{h})$, which respects the properties of symmetry, i.e., $K(u) = K(-u)$ and normalization, i.e., $\int_{-\infty}^{\infty} du K(u) = 1$. The parameter $h > 0$ is the kernel bandwidth. In addition, the maximum of $K(u)$ is obtained for $u = 0$ and $K(u)$ decreases monotonically with $|u|$. This behavior ensures that when estimating the PDF at z , the kernel assigns higher weight to a data value z_n than to a value z_m , if z_n is closer to the target value z than to z_m .

2.1. Probability distribution models for synthetic data

We investigate three non-Gaussian probability distributions commonly associated with precipitation modeling [14]: the gamma (GAM), the Generalized Extreme Value (GEV), and the lognormal (LGN) models. The PDFs of these distributions are given in Eq. (1) below.

$$\text{gamma: } f(z; \xi, \sigma) = \frac{z^{\xi-1} e^{-\frac{z}{\sigma}}}{\sigma^{\xi} \Gamma(\xi)}, \quad z > 0 \text{ and } \xi, \sigma > 0, \quad (1a)$$

$$\text{GEV: } f(z; \mu, \sigma, \xi) = \frac{1}{\sigma} y(z)^{\xi+1} \exp[-y(z)], \quad z \in \mathbb{S}(\xi),$$

$$\text{where } y(z) = \begin{cases} [1 + \xi (\frac{z-\mu}{\sigma})]^{-1/\xi} & \xi \neq 0, \\ \exp(-\frac{z-\mu}{\sigma}) & \xi = 0, \end{cases} \quad (1b)$$

$$\text{lognormal: } f(z; \mu, \sigma) = \frac{1}{z\sigma\sqrt{2\pi}} \exp\left\{-\frac{(\log z - \mu)^2}{2\sigma^2}\right\}, \quad z > 0, \sigma > 0. \quad (1c)$$

In the above equations, $\mu \in \mathbb{R}$ is the location parameter, $\sigma > 0$ is the scale parameter that controls the dispersion of the distribution, and ξ is a shape parameter. $\Gamma(\cdot)$ is the gamma function. Note that for $\xi = 1$, the gamma distribution defaults to the exponential model.

In the case of the GEV distribution, ξ determines which type (I, II, or III) is represented. The Gumbel distribution (type I) is obtained for $\xi = 0$, the Fréchet distribution (type II) for $\xi < 0$, and the Reverse-Weibull distribution (type III) for $\xi > 0$ [50]. For $\xi \in (-0.278, 1)$ the GEV distribution is positively skewed; it also has a finite mean given by $m = \mu + \sigma \frac{\Gamma(1-\xi)-1}{\xi}$ for $\xi \neq 0$,

and $m = \mu + \sigma\gamma_E$ for $\xi = 0$, where $\gamma_E \approx 0.5772$ is the Euler-Mascheroni constant [19]. The support $\mathbb{S}(\xi)$ of the GEV distribution is $\mathbb{S}(\xi) = [\mu - \sigma/\xi, \infty)$ for $\xi > 0$, $\mathbb{S}(\xi) = (-\infty, \infty)$ for $\xi = 0$, and $\mathbb{S}(\xi) = (-\infty, \mu - \sigma/\xi]$ for $\xi < 0$.

The respective CDFs of the gamma, GEV and lognormal models are given below:

$$\text{gamma: } F(z; \xi, s) = \int_0^z f(u; \xi, s) \, du = \frac{\gamma(\xi, \frac{z}{s})}{\Gamma(\xi)}, \quad (2a)$$

$$\text{GEV: } F(z; \mu, \sigma, \xi) = \exp[-y(z)], \quad z \in \mathbb{S}(\xi), \quad (2b)$$

$$\text{lognormal: } F(z; \mu, \sigma) = \frac{1}{2} \left\{ 1 + \operatorname{erf} \left(\frac{\log z - \mu}{\sigma\sqrt{2}} \right) \right\}, \quad \text{for } z > 0. \quad (2c)$$

In Eq. (2), the function $y(z)$ is defined in Eq. (1b), $\gamma(\xi, \cdot)$ represents the lower incomplete gamma function, and $\operatorname{erf}(\cdot)$ is the error function [51]. Also, note that for the gamma and lognormal distributions $F(0; \cdot, \cdot) = 0$, while for the GEV finite values of the CDF are possible for negative values of z . Since $z < 0$ is not acceptable for precipitation amounts, typically one sets $F(z < 0) = 0$ [19].

2.2. Kernel-based CDF estimation

Let $z_{[i]}$ represent the i -th value of the ordered sample, which satisfies the following properties: for any given $i \in \{1, \dots, N\}$ there exists $j \in \{1, \dots, N\}$ such that $z_{[i]} = z_j$ and $z_{[1]} \leq z_{[2]} \leq \dots \leq z_{[N]}$.

The standard PDF kernel density estimator (KDE) is given by

$$\hat{f}_K(z) = \frac{1}{Nh} \sum_{i=1}^N K \left(\frac{z - z_{[i]}}{h} \right), \quad (3)$$

where h is the kernel bandwidth of the kernel $K(\cdot)$.

Non-parametric estimates (KCDE) of the CDF based on kernel functions $K(u)$ can also be obtained. These estimates are given by the following weighted sum

$$\hat{F}_K(z) = \sum_{i=1}^N \frac{1}{N} \tilde{K} \left(\frac{z - z_{[i]}}{h} \right). \quad (4)$$

In Eq. (4), $\tilde{K}(\cdot)$ is the *CDF kernel step* defined by means of the integral

$$\tilde{K}\left(\frac{z - z_{[i]}}{h}\right) = \frac{1}{h} \int_{-\infty}^z dz' K\left(\frac{z' - z_{[i]}}{h}\right). \quad (5)$$

The CDF kernel steps are smoothed versions of the rectangular steps used in the empirical (staircase) CDF estimation. Equation (4) is obtained from Eq. (3) using the integral $\hat{F}_K(z) = \int_{-\infty}^z \hat{f}_K(z') dz'$. Table 1 lists commonly used kernel functions and their respective CDF steps. The CDF step of the Gaussian kernel is evaluated in Section 2.3, while the CDF steps of other commonly used kernels in Appendix A.

A suitable kernel bandwidth h can be estimated by (i) minimizing specific cost functions such as the Root Mean Square Error (RMSE) or the Kullback–Leibler divergence (KLD) between $\hat{F}_K(\cdot)$ and $F(\cdot)$ using leave-one-out cross validation (LOOCV) or (ii) explicit (plug-in) bandwidth formulas based on parametric assumptions [52, 35]. The use of plug-in bandwidths produces similar or better PDF estimates for non-uniformly distributed data than bandwidths estimated with LOOCV [43, 53]. The optimal bandwidth in practice depends on the CDF shape and the data density (i.e., the spacing between measured values) [54]. Our preliminary investigations which compared $\hat{F}_K(z)$ based on (i) the BGK bandwidth and (ii) the LOOCV bandwidth for synthetic data exhibited superior performance of the BGK bandwidth. Hence, we use the plug-in BGK bandwidth derived by [44] as explained in Section 2.4.

In KDE boundary values may require special treatment. For example, large bandwidths can lead to $\hat{F}_K(z) > 0$ for $z < 0$, which is not meaningful for precipitation amounts. Various solutions have been proposed for density estimation near the boundary [55, 56]. Note that it is not permissible to set the PDF equal to zero for $z < 0$, because it would violate the normalization of the PDF. Instead, we modify the CDF so that if $\hat{F}_K(0) = p > 0$, we set $\hat{F}_K(z) = 0$ for $z < 0$ and $\hat{F}_K(0) = p$. This assignment implies zero probability for $z < 0$ and a discontinuous jump at $z = 0$, while it maintains normalization, i.e., $\hat{F}_K(z \rightarrow \infty) = 1$.

2.3. CDF step for Gaussian kernel function

The Gaussian (squared exponential) kernel, defined by $K(u) = \frac{1}{\sqrt{\pi}} \exp(-u^2)$, is an infinitely extended function which has wide-ranging applications in data analysis, machine learning, regression and other fields [57, 58, 59].

Table 1: Kernel functions $K(z)$ and respective CDF kernel steps, $\tilde{K}(u)$, as defined by means of Eq. (5). h is the kernel bandwidth. $\mathbb{I}(|z| \leq 1)$ is an indicator function used for compactly supported kernels: $\mathbb{I}(|z| \leq 1) = 1$ when $|z| \leq 1$ and $\mathbb{I}(|z| \leq 1) = 0$ otherwise. $\text{sgn}(u) = u/|u|$ is the sign function. The following kernel models are used: Ga: Gaussian, Ex: Exponential, Qu: Quadratic, Ep: Epanechnikov, Tr: Triweight, Sp: Spherical, Un: Uniform. For *compact support kernels* (i.e., all but the exponential and Gaussian) the equations for $\tilde{K}(u)$ are valid for $-1 \leq u \leq 1$; for $u < -1$ it holds that $\tilde{K}(u) = 0$, while for $u > 1$ one gets $\tilde{K}(u) = 1$.

Kernel	$K(z)$	$\tilde{K}(u)$ (for compact kernels $ u \leq 1$)
Ga	$\exp(-z^2)$	$\frac{1}{2} [1 + \text{erf}(u)]$
Ex	$\exp(- z)$	$\text{sgn}(u) \frac{1 - e^{- u }}{2} + \frac{1}{2}$
Qu	$\frac{3}{4}(1 - z^2) \mathbb{I}(z \leq 1)$	$\frac{3}{4} \left(u - \frac{u^3}{3} + \frac{2}{3} \right)$
Ep	$\frac{3}{2}(1 - z)^2 \mathbb{I}(z \leq 1)$	$\frac{3}{2} \left(\frac{u^3}{3} - u^2 \text{sgn}(u) + u + \frac{1}{3} \right)$
Tr	$(1 - z^2)^3 \mathbb{I}(z \leq 1)$	$\frac{35}{32} \left(u - u^3 + \frac{3u^5}{5} - \frac{u^7}{7} + \frac{16}{35} \right)$
Sp	$(1 - 1.5 z + 0.5 z ^3) \mathbb{I}(z \leq 1)$	$\frac{4}{3} \left(\text{sgn}(u) \frac{u^2 - 6}{8} u^2 + u + \frac{13}{8} \right)$
Un	$\frac{z}{2} \mathbb{I}(z \leq 1)$	$\frac{1}{2} (u + 1)$

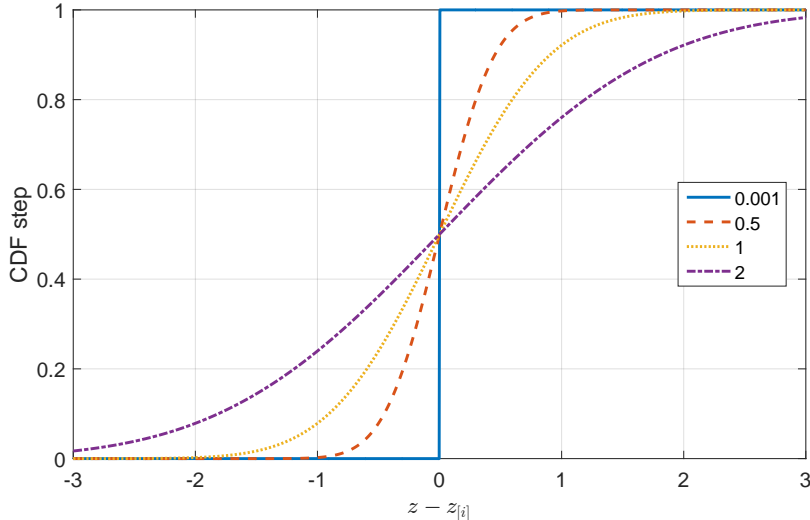


Figure 1: CDF kernel step for the Gaussian kernel based on Eq. (6) for different bandwidths.

Using the change of variable $u_i = (z - z_{[i]})/h$ it follows that $dz = h du_i$. Subsequently, the CDF kernel step $\tilde{K}(u)$ is evaluated by means of the integral

$$\tilde{K}(u_i) = \int_{-\infty}^{u_i} dx K(x) = \frac{1}{2} [\text{erf}(u_i) + 1] , \quad (6)$$

where $\text{erf}(\cdot)$ is the Gauss error function

$$\text{erf}(u_i) = \frac{2}{\sqrt{\pi}} \int_0^{u_i} e^{-x^2} dx .$$

The CDF kernel step obtained from Eq. (6) is illustrated in Fig. 1 for different h values. As shown in these plots, the CDF kernel step tends to the discontinuous step function as $h \rightarrow 0$; then KCDE tends to the empirical staircase estimator. As h increases, the bandwidth becomes smoother.

Results for the CDF kernel steps corresponding to other kernel functions are presented in Table 1; they are based on the calculations in Appendix A. For compactly supported kernels, the step $\tilde{K}(u)$ is zero for $u < -1$, it is given by the expressions listed in Table 1 for $|u| \leq 1$, and it is equal to one for $u > 1$. For kernels with infinite support (e.g., Gaussian, exponential), the kernel step approaches zero and one asymptotically as $u \rightarrow -\infty$ and $u \rightarrow \infty$ respectively.

2.4. BGK bandwidth estimation

The standard bandwidth selection in KDE aims to minimize the Asymptotic Mean Integrated Square Error (AMISE) [35, 40, 54]. Assume a Gaussian kernel $K(\cdot)$ and a PDF $f(z)$ which is at least twice differentiable, i.e., $f'(z)$ and $f''(z)$ are finite numbers for all z . Botev, Grotowski and Kroese [44] (henceforward BGK), have shown that the bandwidth which minimizes AMISE is given by

$$h = \left(\frac{1}{2\sqrt{\pi}N G[f(\cdot)]} \right)^{1/5}, \quad (7)$$

where $G[f(\cdot)] = \int_{-\infty}^{\infty} dz [f''(z)]^2$ is a functional of $f(z)$.

Equation (7) provides the BGK plug-in bandwidth in theory. However, in practice it requires knowledge of the PDF $f(z)$, which is in general unknown *a priori*. BGK approximates $f(z)$ by means of $\hat{f}_k(z)$, which is the KDE based on an auxiliary bandwidth a . The latter is calculated by means of an iterative algorithm after several repetitions [44]. The details of the algorithm are described in Appendix B.

For data that deviate from the normal distribution, the normal reference rule can lead to significant PDF oversmoothing [44, 35, 60, 39]. Another popular method of bandwidth estimation involves using LOOCV to minimise KLD or RMSE between $\hat{F}_K(\cdot)$ and $F(\cdot)$. LOOCV bandwidth estimates require time consuming numerical optimization and often yield small bandwidths that tend to produce peakedness (high kurtosis) in the density [61, 43].

The BGK algorithm has two significant advantages over other plug-in methods: It does not require that the data obey a normal probability model, and it is computed efficiently without the need for numerical optimization [44]. Even though the BGK bandwidth is optimized for the Gaussian kernel, our tests with synthetic data in Section 3 show that it also performs well with compact-support kernels.

3. KCDE Application to Synthetic Data

The KCDE method is applied to synthetic data, the statistical properties of which are motivated by observations of monthly precipitation amounts on the Mediterranean island of Crete (Greece) [29, 46]. One hundred time series of independent values are generated from the gamma, GEV and lognormal

distributions discussed in Section 2.1. Samples of four different sizes ($N=60, 120, 250$ and 600 points) are generated from each distribution.

The studied probability distributions and their parameters are: $\text{GAM}(\xi = 1, \sigma = 30)$, $\text{GAM}(\xi = 0.35, \sigma = 40)$, $\text{GEV}(\xi = 0.25, \sigma = 8, \mu = 15)$, $\text{GEV}(\xi = 0, \sigma = 18, \mu = 45)$, $\text{GEV}(\xi = -0.25, \sigma = 30, \mu = 100)$ and $\text{LGN}(m = 2, \sigma = 1.1)$. The respective theoretical CDFs are shown in Fig. 2 and the PDFs in Fig. 3.

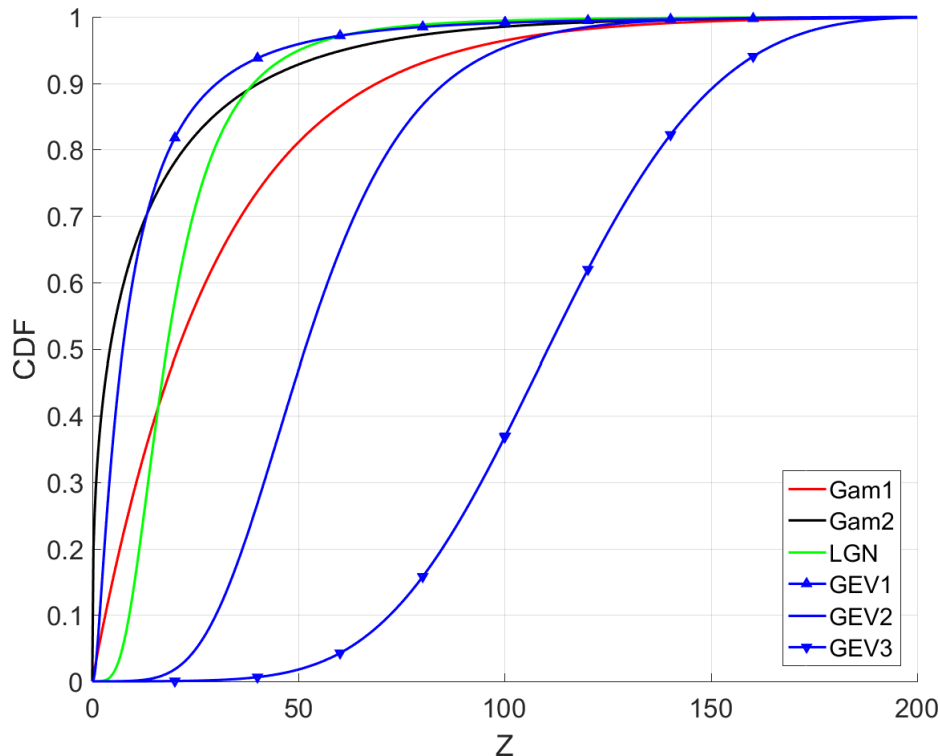


Figure 2: CDF plots for the six investigated probability models [see Eq. (2)]. Gam1: $\text{GAM}(\xi = 1, \sigma = 30)$, Gam2: $\text{GAM}(\xi = 0.35, \sigma = 40)$, GEV1: $\text{GEV}(\xi = 0.25, \sigma = 8, \mu = 15)$, GEV2: $\text{GEV}(\xi = 0, \sigma = 18, \mu = 45)$, GEV3: $\text{GEV}(\xi = -0.25, \sigma = 30, \mu = 100)$, LGN: $\text{LGN}(m = 2, \sigma = 1.1)$. The horizontal axis represents monthly precipitation amount (mm). The parameters ξ, σ, μ for each model are defined with reference to Eq. (1).

3.1. CDF comparisons for synthetic data

The simulated precipitation amounts comprise the vectors $Z_{N;j}^{(m)}$ of length $N \in \{60, 120, 250, 600\}$, $m = 1, \dots, M$ ($M = 100$) denotes the sample index, and $j = 1, \dots, 6$ marks the probability distribution model.

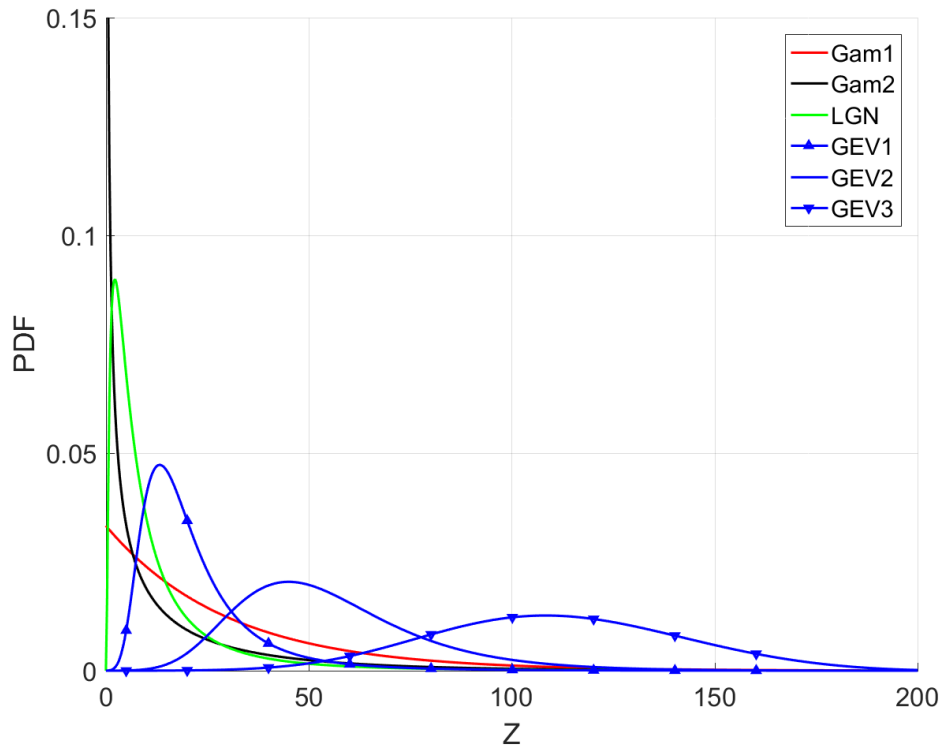


Figure 3: PDF curves for the six investigated probability models [see Eq. (1)]. Gam1: $\text{GAM}(\xi = 1, \sigma = 30)$, Gam2: $\text{GAM}(\xi = 0.35, \sigma = 40)$, GEV1: $\text{GEV}(\xi = 0.25, \sigma = 8, \mu = 15)$, GEV2: $\text{GEV}(\xi = 0, \sigma = 18, \mu = 45)$, GEV3: $\text{GEV}(\xi = -0.25, \sigma = 30, \mu = 100)$, LGN: $\text{LGN}(m = 2, \sigma = 1.1)$. The horizontal axis represents simulated monthly precipitation values (mm). The parameters ξ, σ, μ are defined in the text above Eq. (1).

The CDF is estimated using the KCDE method with the BGK bandwidth (see Section 2). KCDE is performed with several compactly supported kernels (triweight, uniform, spherical, bitriangular, quadratic) and the infinite-support Gaussian kernel. For comparison purposes, in addition to the KCDE, $\hat{F}_K(z)$, we calculate the staircase CDF estimate, $\hat{F}_s(z)$, and the theoretical CDF, $F(z)$, at the test points (times) $t_{k;N,j,m}$, where $k = 1, \dots, N_t$ ($N_t = 500$). The times $t_{k;N,j,m}$ are uniformly distributed between the minimum and maximum values for each sample vector $Z_{N;j}^{(m)}$. In the following, for ease of notation we drop the indices $\{N, j, m\}$ whenever possible.

The mean square error (MSE_k) between $\hat{F}_K(\cdot)$ and the theoretical CDF $F(\cdot)$ is calculated for all the studied kernels and all the samples $Z_{N;j}^{(m)}$ based on the validation values at the test points. Similarly, the mean square error

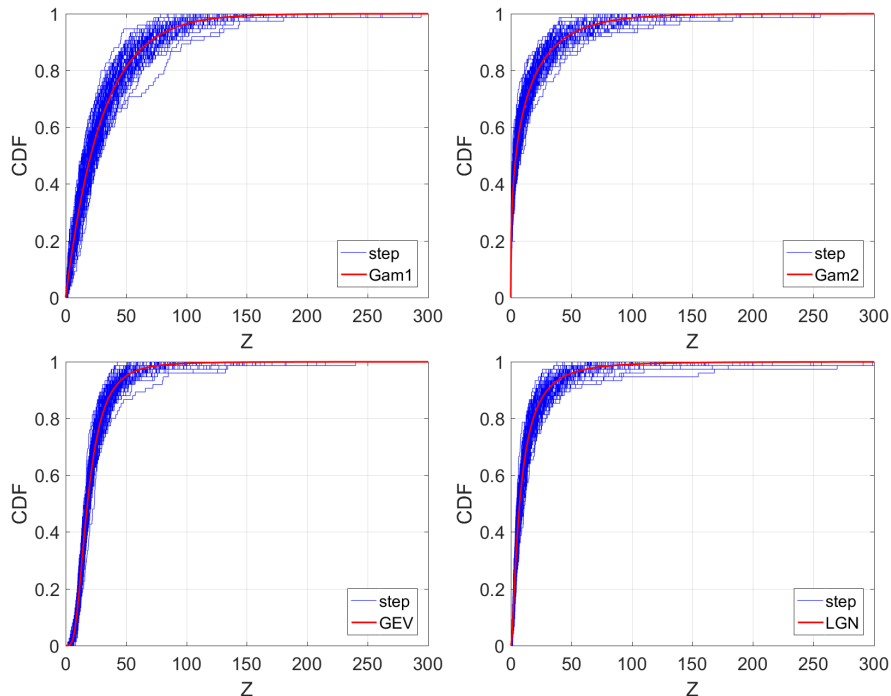


Figure 4: Cloud of 100 empirical (staircase) CDFs for four probability distribution models. Gam1: $\text{GAM}(\xi = 1, \sigma = 30)$, Gam2: $\text{GAM}(\xi = 0.35, \sigma = 40)$, GEV: $\text{GEV}(\xi = 0.25, \sigma = 8, \mu = 15)$, LGN: $\text{LGN}(m = 2, \sigma = 1.1)$. The CDF estimates are based on samples of length $N = 75$. The theoretical CDF curves are shown by the continuous line (red online).

(MSE_s) of the staircase function $\hat{F}_s(\cdot)$ with respect to $F(\cdot)$ is also calculated.

3.2. Analysis of the results

The relative performance of KCDE and the staircase estimate is measured by means of the error ratio $\text{RE}_{k|s} = \frac{\text{MSE}_k}{\text{MSE}_s}$. If $\text{RE}_{k|s} < 1$, the kernel-based CDF $\hat{F}_K(\cdot)$ is a better approximation of the theoretical CDF $F(z)$ than the staircase function. These comparisons are illustrated in the box plots of Figs. 5-10. The following abbreviations are used: ‘‘Gam’’ refers to the Gamma(ξ, σ) distribution. Gam1: ($\xi = 1, \sigma = 30$), Gam2: ($\xi = 0.35, \sigma = 40$). ‘‘GEV’’ refers to the generalized extreme value distribution (ξ, σ, μ). GEV1($\xi = 0.25, \sigma = 8, \mu = 15$), GEV2($\xi = 0, \sigma = 18, \mu = 45$), GEV($\xi = -0.25, \sigma = 30, \mu = 100$). ‘‘LGN’’ refers to the lognormal distribution with $m = 2$ and $\sigma = 1.1$. As evidenced in these plots, in most cases the KCDEs, $\hat{F}_K(z)$, perform better than the staircase estimates $\hat{F}_s(z)$. Hence, $\hat{F}_K(z)$, especially

for compact kernels, better approximates the CDF of non-Gaussian, skewed distributions than the staircase CDF $\hat{F}_s(z)$. The exception is GAM($\xi = 0.35$, $\sigma = 40$), the PDF $f(z)$ of which exhibits a singularity at zero (see Fig. 3). This violates the BGK smoothness conditions which require the existence of $f'(z)$ and $f''(z)$.

Based on Figs. 5-10, no single kernel is universally the top performer. The compact kernels tend to outperform the Gaussian kernel but not in every case. In our tests, the Gaussian kernel performs better than all the compact kernels in 40.5% of the 2400 experiments, particularly for the GEV distribution. The Epanechnikov and uniform kernels performed best among the compact kernels, with Epanechnikov returning the smallest $\text{RE}_{\text{k|s}}$ in 21.0% and the uniform kernel performing best in 22.2% of the 2400 experiments. The spherical kernel, while performing well compared to the step function (see Fig. 5), performed best among all kernels only in 1.3% of the experiments. Nonetheless, deviations of the spherical from other compact kernels in terms of MSE were within 2% (based on the average MSE over the 24 different sampling scenarios). In most cases in which the spherical kernel performs well, a different kernel performs slightly better (often the Epanechnikov kernel).

The same analysis was performed using the plug-in bandwidth $r_{N;j}^{(m)}$ based on the normal reference rule:

$$r_{N;j}^{(m)} = 1.06\sigma_j^{(m)}N^{-1/5}, \quad m = 1, \dots, M, \quad j = 1, \dots, 6, \quad (8)$$

where $\sigma_j^{(m)}$ is the standard deviation of the sample $Z_{N;j}^{(m)}$ [40]. The results (Figs. C1–C5 in Appendix C) show that \hat{F}_K using the normal reference bandwidth performs similarly to the staircase estimate \hat{F}_s for all compact kernels. The BGK bandwidth $h_{N;j}^{(m)}$ outperforms the normal reference rule according to the error ratio $\text{RE}_{\text{k|s}}$. The results support the conclusions reached in [44].

The above analysis shows that KCDE equipped with the BGK bandwidth estimates the CDF of synthetic data more reliably than KCDE with the normal reference bandwidth and the empirical staircase estimators. The relative performance of different kernel functions on the estimate of the CDF $\hat{F}_K(z)$ should be further investigated.

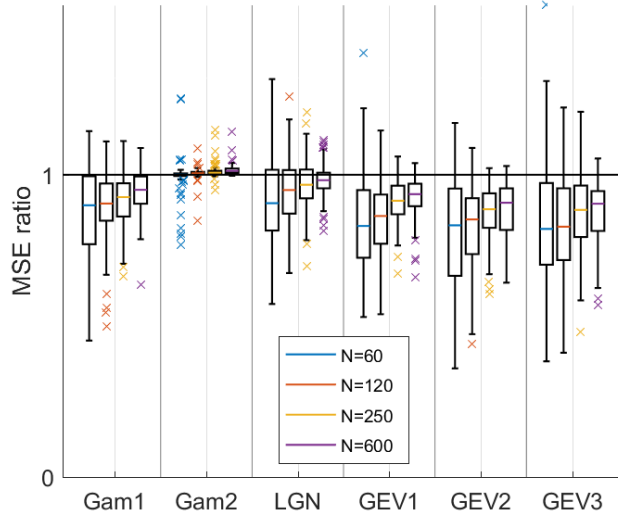


Figure 5: Boxplots of $RE_{k|s}$ (MSE of KCDE \hat{F}_K divided by the MSE of the staircase estimate \hat{F}_s) for the spherical kernel. N is the sample size. The abbreviations of the probability models (Gam1, Gam2, LGN, GEV1, GEV2, GEV3) are defined in the main text.

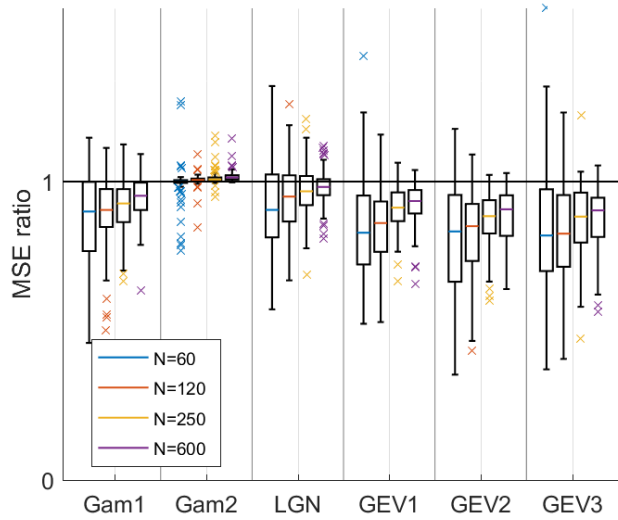


Figure 6: Boxplots of $RE_{k|s}$ (MSE of KCDE \hat{F}_K divided by the MSE of the staircase estimate \hat{F}_s) for the triweight kernel. N is the sample size. The abbreviations of the probability models (Gam1, Gam2, LGN, GEV1, GEV2, GEV3) are defined in the main text.

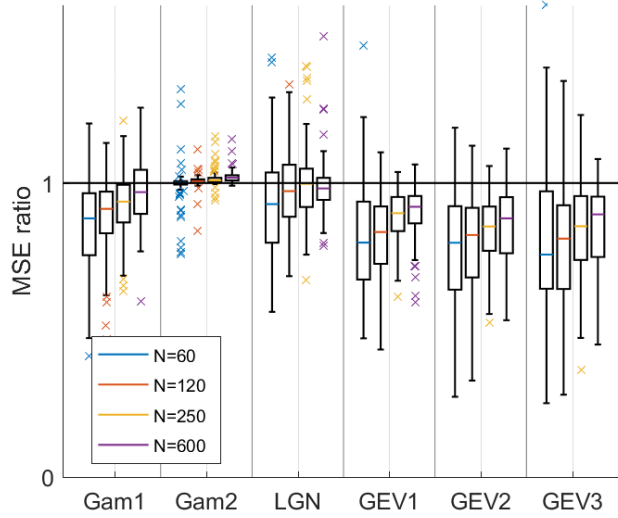


Figure 7: Boxplots of $RE_{k|s}$ (MSE of KCDE \hat{F}_K divided by the MSE of the staircase estimate \hat{F}_s) for the quadratic kernel. N is the sample size. The abbreviations of the probability models (Gam1, Gam2, LGN, GEV1, GEV2, GEV3) are defined in the main text.

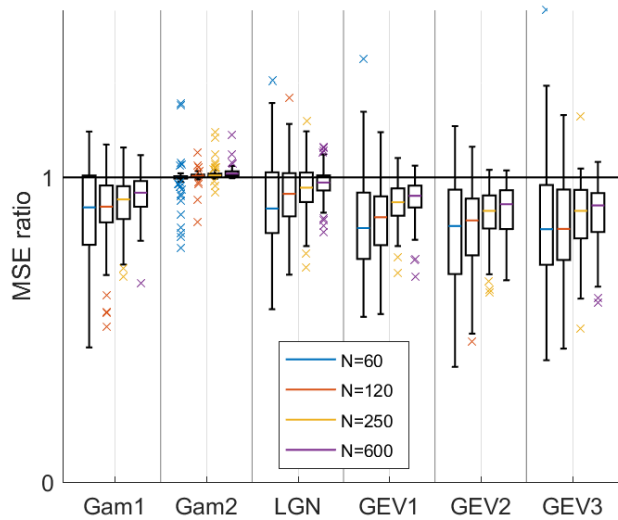


Figure 8: Boxplots of $RE_{k|s}$ (MSE of KCDE \hat{F}_K divided by the MSE of the staircase estimate \hat{F}_s) for the Epanechnikov kernel. N is the sample size. The abbreviations of the probability models (Gam1, Gam2, LGN, GEV1, GEV2, GEV3) are defined in the main text.

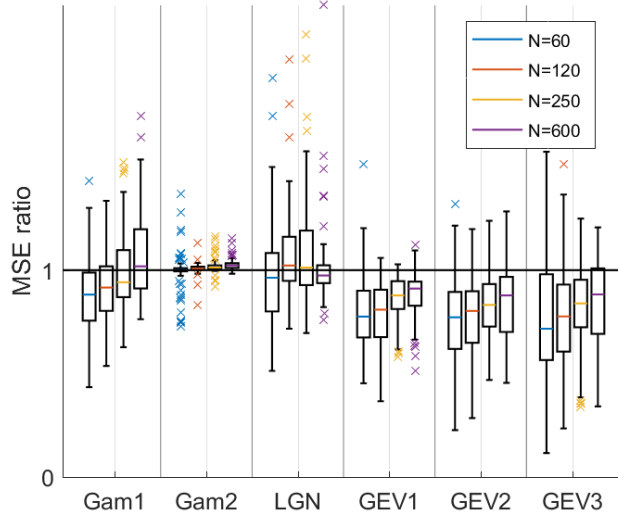


Figure 9: Boxplots of $RE_{k|s}$ (MSE of KCDE \hat{F}_K divided by the MSE of the staircase estimate \hat{F}_s) for the uniform kernel. N is the sample size. The abbreviations of the probability models (Gam1, Gam2, LGN, GEV1, GEV2, GEV3) are defined in the main text.

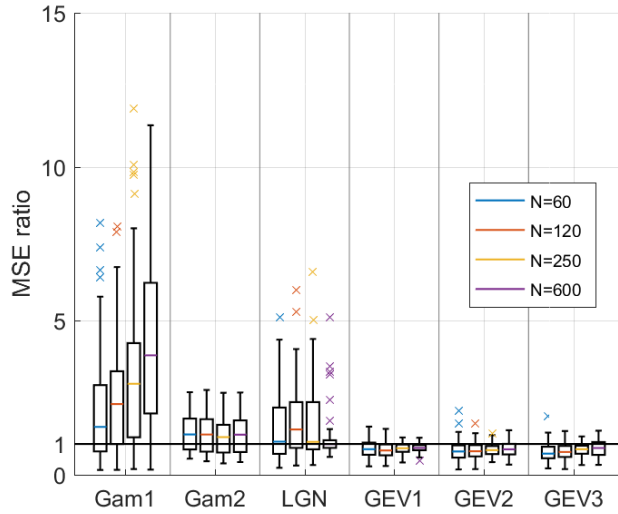


Figure 10: Boxplots of $RE_{k|s}$ (MSE of KCDE \hat{F}_K divided by the MSE of the staircase estimate \hat{F}_s) for the Gaussian kernel. N is the sample size. The abbreviations of the probability models (Gam1, Gam2, LGN, GEV1, GEV2, GEV3) are defined in the main text.

4. KCDE Application to Reanalysis Data

The second data set involves ERA5 reanalysis precipitation data (mm) downloaded from the Copernicus Climate Change Service [62]. The data set includes 23,360,610 values of hourly precipitation amounts for a period of 41 years (from 01-Jan-1979 06:00:00 to 31-Dec-2019 23:00:00) at the nodes of a 5×13 spatial grid (see Fig. 11) on and around the island of Crete (Greece). The average spatial resolution is ≈ 0.28 degrees (grid cell size ≈ 31 km), and 359,394 hourly precipitation values are available at every node.

Our analysis focuses on the wet period, i.e., from October to March [63]. Daily, weekly, monthly and annual precipitation sets were generated by aggregating the hourly values at each location over the respective time window. Zero values in each set were replaced with random numbers uniformly distributed in the interval $[eps, z_{\min}]$, where eps is the floating-point relative accuracy of the computer ($eps = 2.2204 \times 10^{-16}$). This transformation allows fitting the data to parametric distributions with no probability mass at zero, e.g., the lognormal distribution. In addition, it circumvents the reduced performance of KCDE with such data, exemplified by the analysis of the gamma distribution with $\xi = 0.35$ in Section 3. The strategy of replacing zeros with small values is used in various studies of precipitation [4, 64, 65]. To investigate the impact of the replacement scheme, we tested replacing zeros with eps and with random selection between eps and z_{\min} . We found that the replacement scheme did not significantly impact the estimated probability distributions.

4.1. CDF comparisons for the ERA5 data

The KCDE analysis of precipitation data was performed for all 65 grid nodes. For brevity we mostly discuss results from a single representative node (see Fig. 11) which is located near the major agricultural area of Crete, i.e., the valley of Messara [67]. The coordinates (LAT, LON) of the test node in the World Geodetic System (WGS 84) are $35^{\circ}0'0.00''$ N and $25^{\circ}0'0.00''$ E. The distributions at 5 additional nodes, geographically dispersed over the island, are considered in the simulation study in Section 5.

Table 2 presents summary statistics of wet-period precipitation amounts for the four time scales along with the respective best-fit parametric models based on BIC. The optimal parametric models are all non-Gaussian distribution.

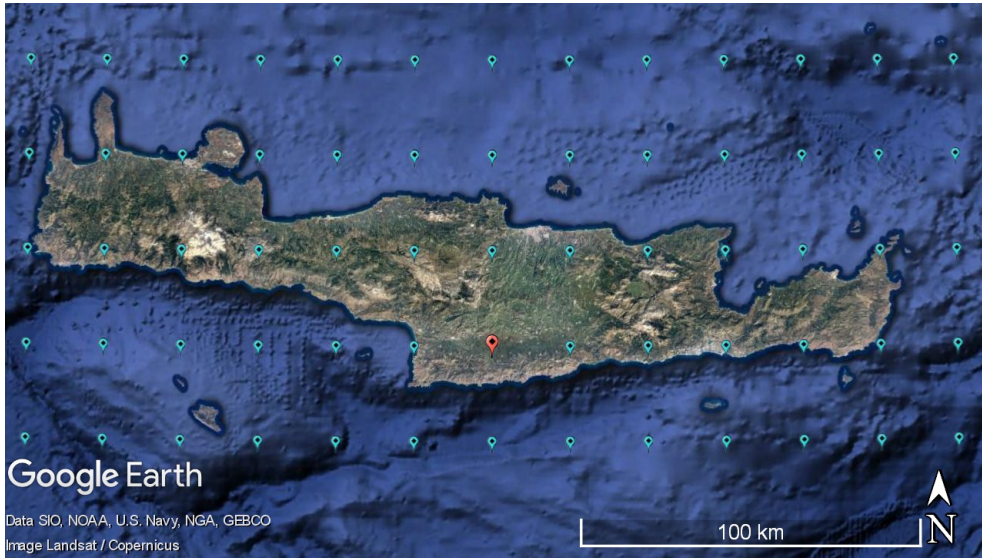


Figure 11: Geomorphological map of Crete showing the 65 ERA5 grid locations (blue markers) on and around the island of Crete (Greece) used in this study [66]. The node on the fourth row and seventh column (red marker online) is the test location near the Messara valley.

Table 3 extends the analysis presented in Table 2 by reporting the optimal parametric model based on three different criteria: Akaike’s Information Criterion (AIC), the Bayesian Information Criterion (BIC), and the negative log likelihood (NLL). The three criteria agree on the optimal distribution for all time scales. For daily amounts the optimal fit is obtained by the Weibull, followed by the gamma, lognormal, GEV and the normal distribution. For weekly precipitation, the ranking of the probability distributions (from best to worst) is: gamma, Weibull, lognormal, GEV and normal. For the monthly data, the following ranking is obtained: Weibull, gamma, GEV, normal, and lognormal. Finally, for the annual data the best model is the Weibull distribution.

Table 4 reports the frequency (number of ERA5 nodes) with which a parametric model is selected as the optimal probability distribution for each time scale. As in the case of the test location, all three criteria agree on the optimal model except for the annual time scale. On the daily scale, the gamma model is selected at 38 nodes, followed by the Weibull model at 27 nodes. For the weekly scale the gamma distribution is the optimal model at all 65 nodes. For the monthly scale, the Weibull distribution is the optimal

Table 2: Summary statistics for the daily, weekly, monthly and annual precipitation amounts for the wet period (October to March) (from ERA5 reanalysis data) for the test location on the island of Crete. The coordinates (LAT, LON) of the node are $35^{\circ}0'0.00''\text{N}$ and $25^{\circ}0'0.00''\text{E}$ in the World Geodetic System (WGS 84). N : Number of records, N_z : number of zero records before replacement, \bar{z} : mean value, $z_{0.50}$: median, z_{\min} : minimum, z_{\max} : maximum, σ_z : standard deviation, cov : coefficient of variation, s_z : skewness, k_z : kurtosis. “Model” is the best-fit distribution based on the Bayesian Information Criterion (BIC).

Scale	N	N_z	\bar{z}	$z_{0.50}$	z_{\min}	z_{\max}	σ_z	cov	s_z	k_z	Model
Daily	7,472	1,808	1.5832	0.1054	5.4538×10^{-8}	56.1037	3.9379	2.4874	4.9374	36.4806	Weibull
Weekly	1,068	13	11.1408	6.3019	5.4538×10^{-8}	84.3720	12.6018	1.1311	1.5805	5.5087	gamma
Monthly	246	0	48.0850	44.3109	0.8783	142.1008	29.4220	0.6119	0.6378	3.0325	Weibull
Annual	41	0	288.5103	303.1404	163.4173	445.0781	66.7700	0.2314	-0.1206	2.5123	Weibull

Table 3: Best-fit probability distribution models for the daily, weekly, monthly and annual precipitation amounts for the wet period (October to March) (from ERA5 reanalysis data) for the selected node near Messara valley. Measures of fit: Akaike’s Information Criterion (AIC), the Bayesian Information Criterion (BIC), and the negative log-likelihood (NLL). Measures of fit for the optimal models are boldfaced.

Method \ Model	Normal	Weibull	gamma	GEV	LGN
Daily precipitation					
AIC	4.1691×10^4	-6.0611×10^3	-5.9517×10^3	-4.3285×10^3	-5.6557×10^3
BIC	4.1704×10^4	-6.0473×10^3	-5.9379×10^3	-4.3078×10^3	-5.6418×10^3
NLL	2.0843×10^4	-3.0326×10^3	-2.9779×10^3	-2.1673×10^3	-2.8298×10^3
Weekly precipitation					
AIC	8.4461×10^3	6.9698×10^3	6.8849×10^3	7.5483×10^3	7.5165×10^3
BIC	8.4561×10^3	6.9797×10^3	6.8948×10^3	7.5632×10^3	7.5264×10^3
NLL	4.2211×10^3	3.4829×10^3	3.4404×10^3	3.7712×10^3	3.7562×10^3
Monthly precipitation					
AIC	2.3649×10^3	2.3276×10^3	2.3428×10^3	2.3406×10^3	2.3996×10^3
BIC	2.3719×10^3	2.3346×10^3	2.3467×10^3	2.3531×10^3	2.4066×10^3
NLL	1.1832×10^3	1.1618×10^3	1.1678×10^3	1.1673×10^3	1.1988×10^3
Annual precipitation					
AIC	463.8558	463.4259	465.4719	467.1305	465.8434
BIC	467.2829	466.8531	468.8991	470.8069	470.6502
NLL	230.7360	229.7130	231.5652	229.9199	229.9217

model at most nodes according to all three criteria (the number of nodes differs depending on the criterion). Finally, for the annual precipitation AIC and BIC select the gamma model at 28 nodes, the normal at 18 nodes, the lognormal at 14 nodes and the Weibull at 5 nodes. For the annual data, the Weibull distribution provides the best fit at the test location (and its four nearest nodes in the south), while the gamma distribution is selected at the majority of the ERA5 sites.

4.2. KCDE of precipitation amount at different time scales

From the analysis above it follows that the optimal parametric model depends on both the time scale considered and the geographic location. This variability motivates the use of non-parametric estimates of the underlying probability distribution. This section presents KCDEs of precipitation amount at the test location over the daily, weekly, monthly and annual time windows.

The KCDEs are calculated with the Epanechnikov kernel which performed best (among the studied compact kernels) on synthetic data, as discussed in Section 3. The sample size for each time window is shown in Table 2. Figure 12 compares the empirical (staircase), and KCDE estimates with the best-fit parametric models for each time scale. As is evident in these plots, the continuous KCDE curves are closer to the empirical estimates than the parametric models. The behavior reflects the fact that parametric models are not flexible enough to capture the natural stochasticity of precipitation. The differences between the three curves are smallest in the case of the annual data, which are closer to the normal distribution (see Table 4). The respective BGK bandwidths for the Epanechnikov kernel are $h_d = 7.5786 \times 10^{-4}$, $h_w = 9.4512 \times 10^{-3}$, $h_m = 14.898$, and $h_a = 40.824$ (all in mm) for the four different time scales. These results show that the BGK bandwidth adapts to the shape and scale of the underlying distribution. The inset plots in Fig. 12 demonstrate that KCDE provides estimates closer to the empirical CDF than the optimal parametric models. Note that the BGK bandwidth for the monthly wet-season data is $h_m = 14.898$ mm while the respective bandwidth for the monthly entire-season data set is $h_m = 0.1051$ mm (the analysis for the entire season is not reported herein). This difference is due to the presence of a large number of zero values in the full data set and illustrates the ability of the BGK bandwidth to adapt to the data distribution.

Table 4: Number of times $\in [0 - 65]$, a parametric model is selected as the optimal distribution for the daily, weekly, monthly and annual precipitation amounts for the wet period (October to March) for the 65 ERA5 nodes around Crete. Measures of fit: Akaike’s Information Criterion (AIC), the Bayesian Information Criterion (BIC), and the negative log-likelihood (NLL). Measures of fit for the optimal models are boldfaced.

Method	Model	Normal	Weibull	gamma	GEV	LGN
	Daily precipitation					
AIC		0	27	38	0	0
BIC		0	27	38	0	0
NLL		0	27	38	0	0
Weekly precipitation						
AIC		0	0	65	0	0
BIC		0	0	65	0	0
NLL		0	0	65	0	0
Monthly precipitation						
AIC		0	61	4	0	0
BIC		0	61	4	0	0
NLL		0	59	1	5	0
Annual precipitation						
AIC		18	5	28	0	14
BIC		18	5	28	0	14
NLL		3	2	7	52	1

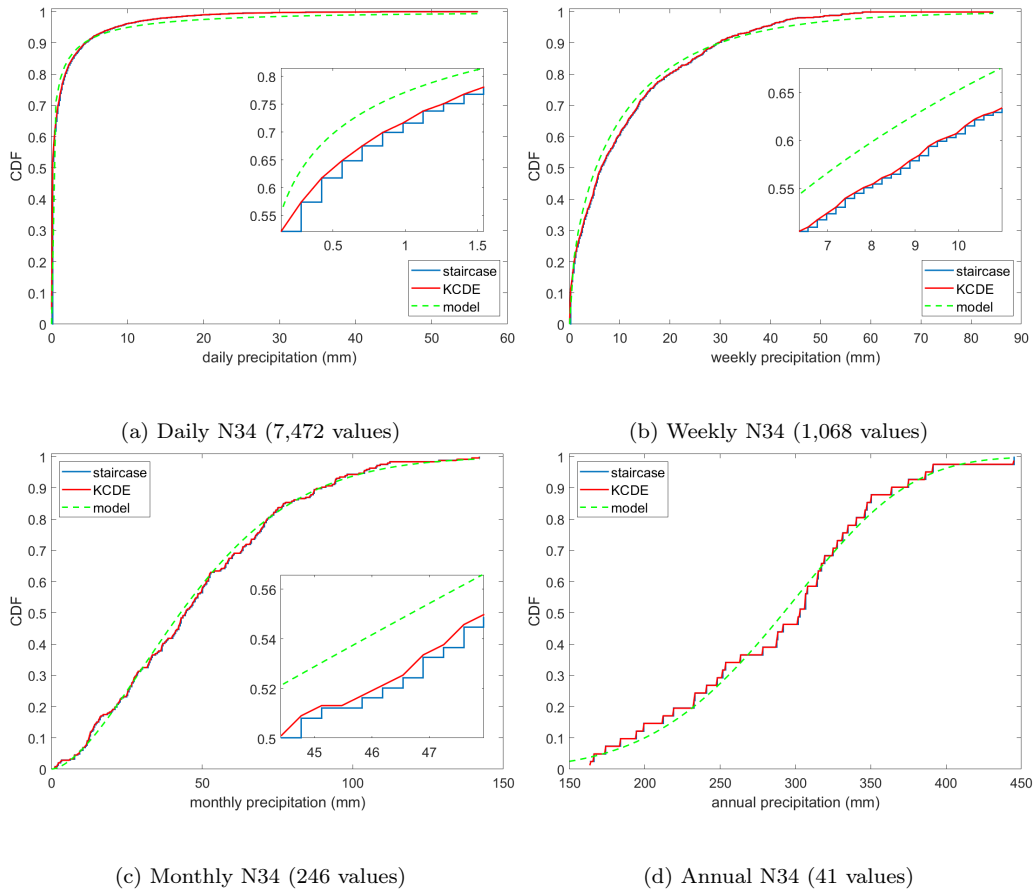


Figure 12: Empirical–staircase (step function, blue online) and KCDE with Epanechnikov kernel (smooth line, red online) CDF estimates for the daily (upper left), weekly (upper right), monthly (bottom left) and annual (bottom right) precipitation amount reanalysis data for the wet period (October to March). The dashed line (green online) corresponds to CDFs of the optimal parametric models based on the Bayesian Information Criterion (BIC). Based on BIC, the optimal models are Weibull (daily), gamma (weekly), Weibull (monthly), and Weibull (annual) scales respectively.

5. Simulation Algorithm for Rainfall Amount

Time series of rainfall amount that respect KCDE-derived distributions can be simulated using the *inverse transform sampling (ITS) method* [49]. Given a time series of precipitation amounts (z_1, z_2, \dots, z_N) , the goal is to generate an ensemble of time series, $(z_1^{(m)}, z_2^{(m)}, \dots, z_{N'}^{(m)})$, $m = 1, \dots, M$, that share the same probability distribution as the sample. Henceforth we

drop the state index (m) to abbreviate notation.

The ITS method is based on the law of conservation of probability under nonlinear, monotonic transformations: If $Z(\omega)$ is a random variable with CDF $\hat{F}_Z(z)$ and $U(\omega)$ is a uniformly distributed random variable, then

$$\hat{F}_Z(z) = F_U(u) = u \Rightarrow z = \hat{F}_Z^{-1}(u), \quad (9)$$

where $F_U(\cdot)$ is the CDF of the uniform distribution. The inverse CDF $\hat{F}_Z^{-1}(\cdot)$ can be calculated either by means of numerical optimization or a lookup table; we use the latter approach. For compactly supported kernel functions, ITS simulation involves the following steps:

1. The KCDE-based CDF of precipitation amount $\hat{F}_Z(z)$ is derived from the sample by applying Eq. (4).
2. A lookup table is generated which comprises a set of $L = 10,000$ discretization points, i.e., $\{(z_l, u_l)\}_{l=1}^L$ pairs.
3. The set $\{z_l\}_{l=1}^L$ is obtained by uniformly distributing $z_l \in [z'_{\min}, z'_{\max}]$, where $z'_{\min} = \max(\text{eps}, z_{\min} - h)$, $z'_{\max} = z_{\max} + h$, z_{\min} , z_{\max} are respectively the minimum and maximum values of the available sample, and h is the BGK bandwidth.
4. The set $\{u_l\}_{l=1}^L$ is generated by setting $u_l = \hat{F}_Z(z_l)$, for all $l = 1, \dots, L$ according to Eq. (9).
5. A set of uniform random numbers $\{u_n\}_{n=1}^{N'} : u_n \stackrel{d}{=} U(0, 1)$ are generated.
6. For each u_n , $n = 1, \dots, N'$ the nearest neighbor $u_{l|n}$ in the lookup table is found, and the simulated value z_n is set equal to $z_{l|n}$, i.e., which is the pair of $u_{l|n}$ in the lookup table.

5.1. Simulations based on parametric probability distributions

One simulated state was generated for each probability model in Section 2.1, based on a sample of length $N = 250$. The simulated time series involve $N' = 250$ points. The CDF $\hat{F}_k(\cdot)$ was estimated using Eq. (4) with the spherical kernel (which has similar performance as the Epanechnikov kernel; see Section 3.2)

Figure 13 shows the quantile-quantile (q-q) plots between the simulated series and the samples. The q-q pairs cluster around the diagonal line, indicating good agreement between the probability distributions of the sample

and simulated state, except for a few points in the right tail of the distributions. This behavior signifies underestimation of the maxima by the ITS simulated time series. Given the skewness of the probability models (as discussed in Section 3), the bias stems from the fact that obtaining a simulated sample which contains a value close to the maximum value of the sample requires generating a uniform random number close to one. This is more likely to happen for simulated series of greater length. Note that values higher than the sample maximum can also be obtained by ITS simulation and are more likely for high values of N' compared to N (this case is not shown herein). For compactly supported kernels such values do not exceed the limit $z_{\max} + h$.

5.2. Simulations based on ERA5 reanalysis data

Wet-period ERA5 daily precipitation data (see Sec. 4) from 1979 to 2019 at six geographically dispersed nodes are used to demonstrate the application of the ITS simulation method. The selected locations are listed in Table 5.

Table 5: List of the selected ERA5 nodes. The node coordinates (LAT, LON) are shown in the World Geodetic System (WGS 84).

Index s	Node	Area Name	(LAT, LON)
$s = 1$	N12	Chania	(35°30'0.00" N, 24°00'0.00" E)
$s = 2$	N13	Lefka Ori (White Mountains)	(35°15'0.00" N, 24°00'0.00" E)
$s = 3$	N18	Askifou plateau	(35°15'0.00" N, 24°15'0.00" E)
$s = 4$	N28	Psiloritis mountain	(35°15'0.00" N, 24°45'0.00" E)
$s = 5$	N34	Vagionia	(35°00'0.00" N, 24°00'0.00" E)
$s = 6$	N49	Ierapetra	(35°00'0.00" N, 25°45'0.00" E)

The time series $Z_{N;s,t}$, where $t = 1, \dots, 41$, and $s = 1, \dots, 6$ denotes the precipitation amount for the wet period of a specific year (indexed by $t = \text{year} - 1978$) at a specific node (denoted by s). For example, the time series $Z_{182;4,1}$ refers to location $s = 4$ and year 1979 and comprises $N = 182$ values corresponding to the wet-period days. Aggregate time series, $Z_{N;s}$, comprise the wet-period data for the entire 41-year window at each location.

The CDF estimates $\hat{F}_{K;s}(z)$ for $Z_{N;s}$ and $\hat{F}_{K;s,t}(z)$ for $Z_{N;s,t}$, for $s = 1, \dots, 6$ and $t = 1, \dots, 41$ were calculated using the Epanechnikov kernel with the BGK bandwidth (which are henceforth used). The results are shown in Fig. 14. All CDFs have similar shape which is different from the s-shaped normal CDF. The CDFs exhibit significant probability mass for small values

and an extended right tail. The maximum amount differs slightly between locations.

To test the ITS simulation method we used the following study design. For each of the years 2015–2019 ($t = 37, \dots, 41$), the time series $Z_{N;s,t}$ for the years $t = 1, \dots, T - 1$ were used as the training set. The precipitation time series $Z_{N;s,T}$ for the year $t = T$ were considered as the validation set. For each year, an aggregate time series $Z_{N;s}$ was constructed based on the data of the respective training set. Based on the latter, 1000 times series for the year T were simulated using ITS. The simulated time series are denoted by $Z_{N;s,t}^{(m,T)}$, where $t = 1, \dots, T - 1$, $m = 1, \dots, 1000$ is the state index, $s = 1, \dots, 6$ and $T = 37, \dots, 41$ is the index of the validation year.

5.3. Analysis of simulations based on ERA5 data

Figures 15-16 present boxplots of total precipitation during the wet period of the validation year (on the left column) as well as the maximum daily precipitation (on the right column). These boxplots are based on the 1000 simulated states for each node s and validation year T . The respective wet-period total and maximum daily precipitation validation values for each year T are also shown (using longer horizontal line segments).

In most cases, the validation values are within the distributions generated by ITS simulation. For the wet-season total precipitation, the simulations generated reliable predictions at all locations with the exception of the year 2019 ($T = 41$). In 2019 the data at the first three stations, which are located on the Western side of the Crete, exceed the range generated by ITS. The year 2019 was marked by extremely heavy precipitation on Crete [68], and the western part of the island typically receives most of the precipitation. Hence, it is not surprising that the simulation, which was trained on previous years of less intense precipitation, did not adequately capture the behavior for 2019.

Regarding estimates of the expected daily maximum precipitation, the 95% percentile of the ITS simulations seems adequate. For the six studied locations and the five validation years, the validation ERA5 maximum value exceeded the 95% interval only in Chania ($s = 1$) during 2019 ($T = 41$).

It should be noted that precipitation estimates at different locations are spatially correlated. Thus 2016 was a rather dry year while 2019 a particularly wet year for all locations. This behavior reflects the spatial correlation inherent in the reanalysis data.

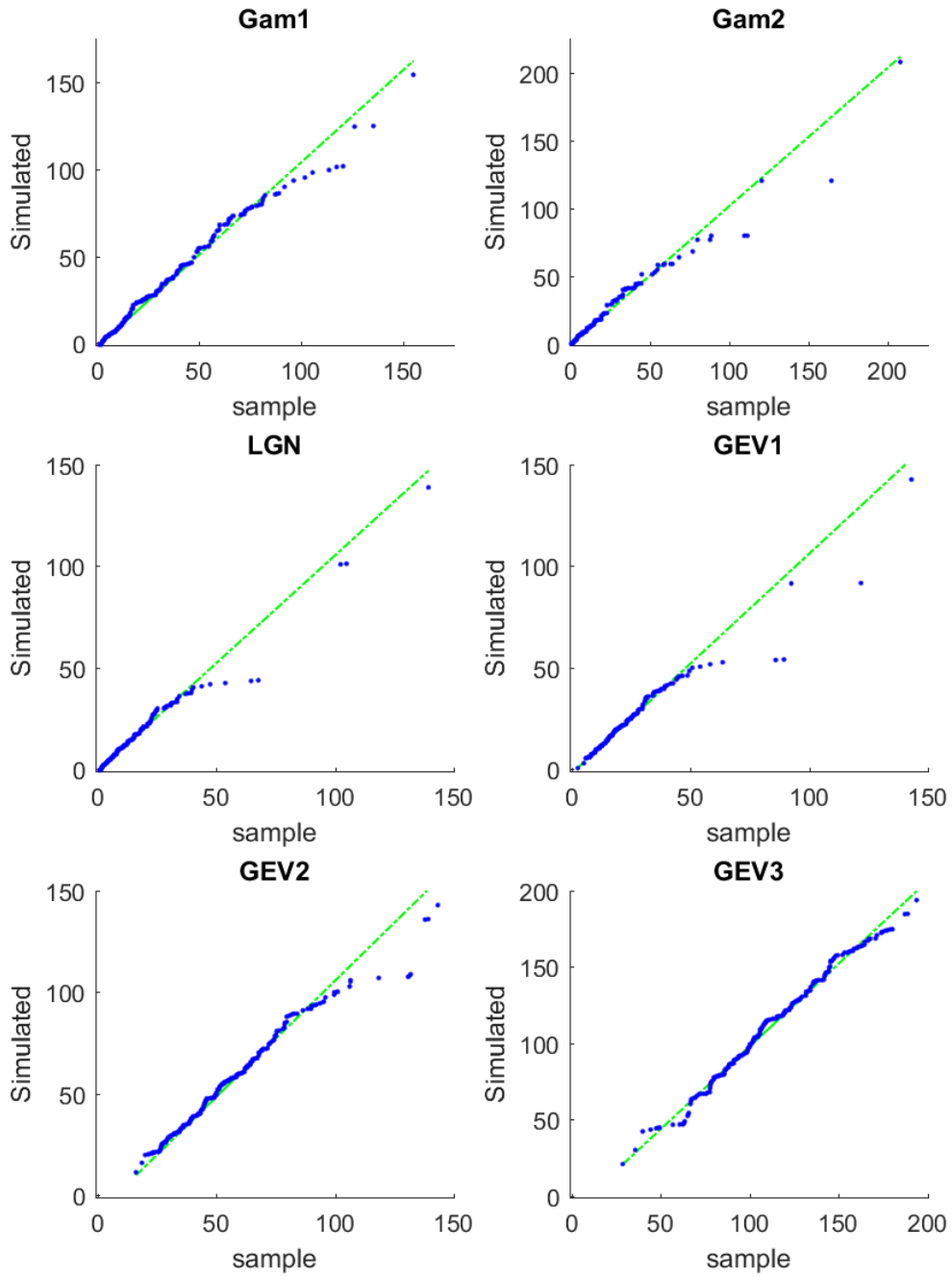


Figure 13: Quantile-quantile (q-q) plots between synthetic sample data and ITS simulated sequences of the same length. The kernel-based CDF estimate \hat{F}_k was constructed using the spherical kernel. Each synthetic sample includes 250 values drawn from the parametric probability distributions presented in Section 2.1.

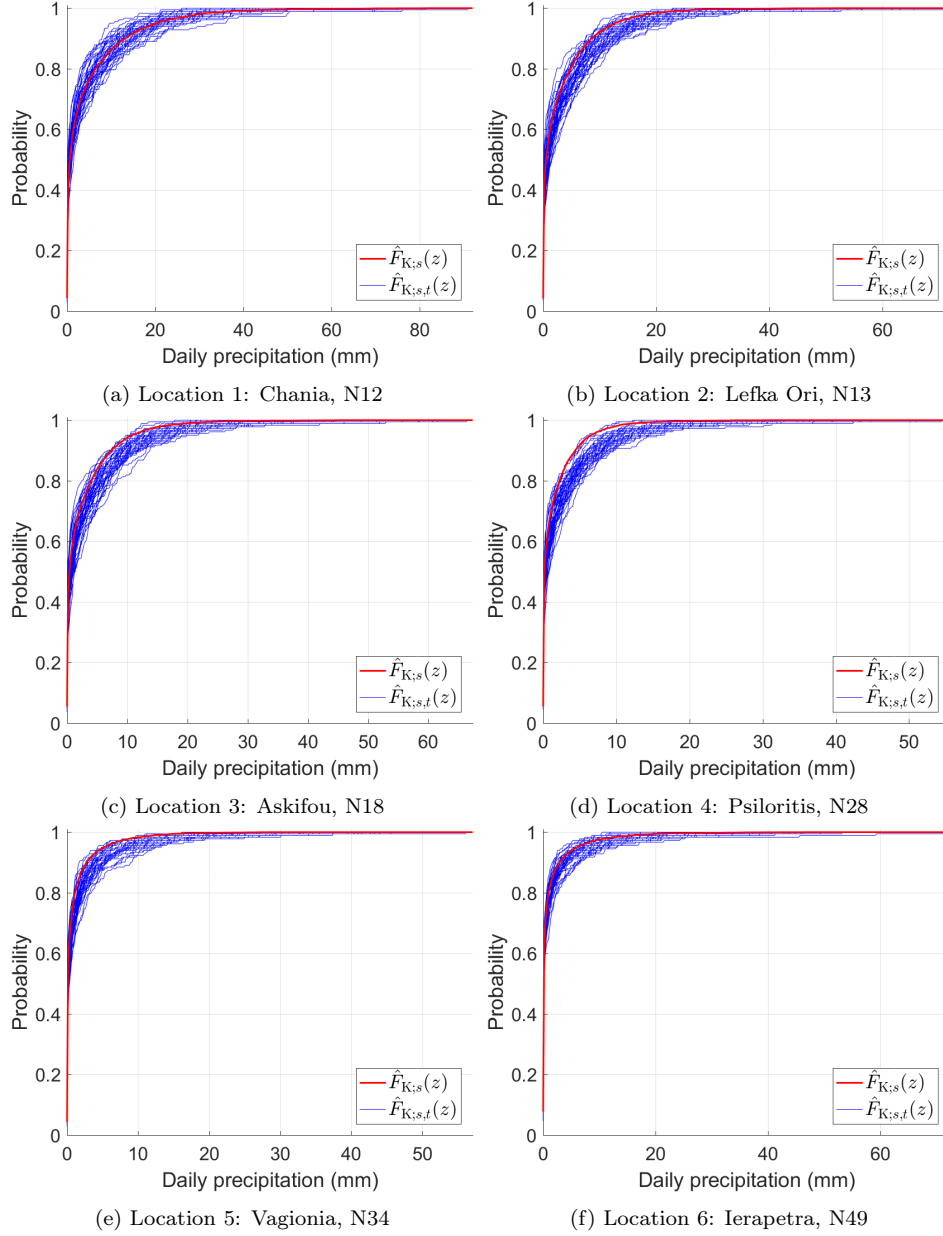


Figure 14: CDF $\hat{F}_{K;s,t}(z)$ clouds for precipitation amount of individual years (blue lines) and $\hat{F}_{K;s}(z)$ for the aggregate precipitation (red lines) at six ERA5 nodes. The Epanechnikov kernel with BGK bandwidth was used for CDF estimation.

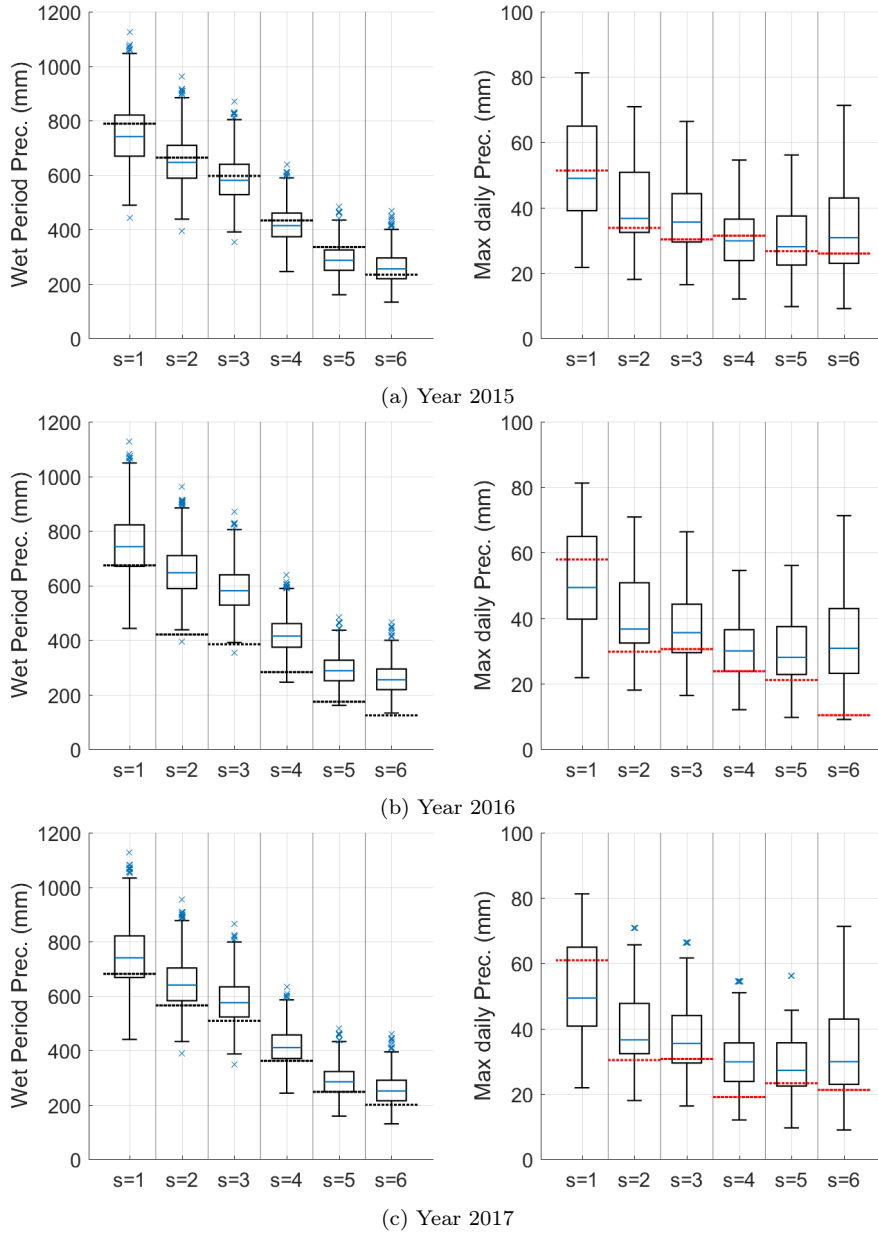


Figure 15: Boxplots of wet-period total (left column) and maximum daily (right column) precipitation based on 1000 ITS simulations at six ERA5 nodes: s_1 : Chania, s_2 : Lefka Ori, s_3 : Askifou, s_4 : Psiloriths, s_5 : Vagionia, s_6 : Ierapetra. Dotted horizontal lines extending outside the boxes represent the total (black, left column) and maximum daily (red, right column) ERA5 precipitation values for the validation years 2015-2017.

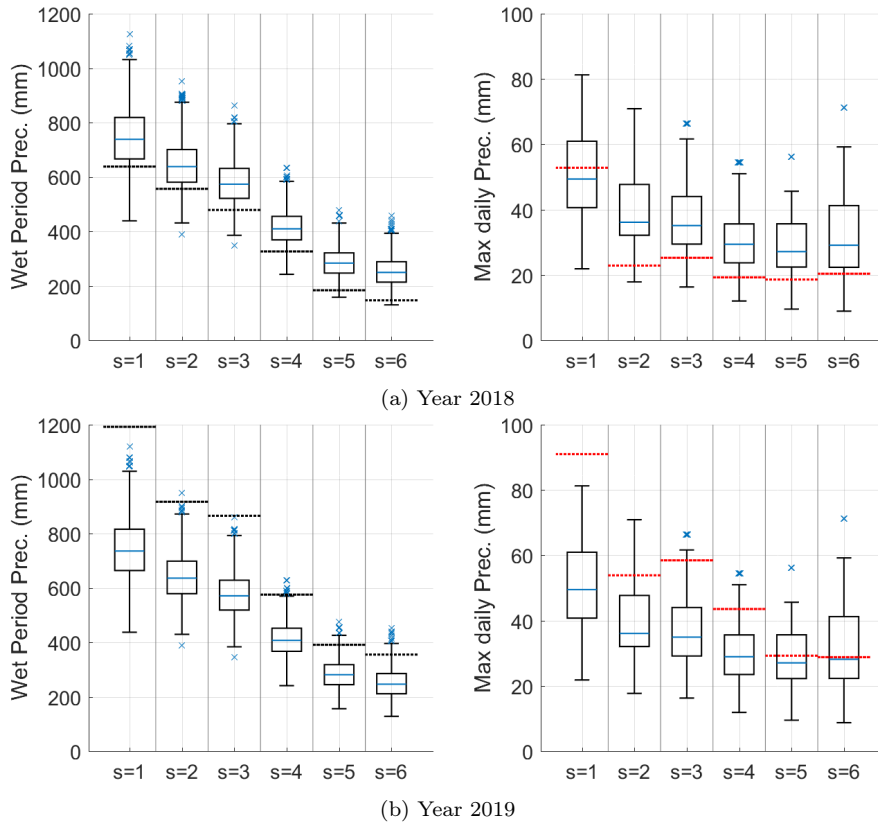


Figure 16: Boxplots of wet-period total (left column) and maximum daily (right column) precipitation based on 1000 ITS simulations at six ERA5 nodes: s_1 : Chania, s_2 : Lefka Ori, s_3 : Askifou, s_4 : Psiloriths, s_5 : Vagionia, s_6 : Ierapetra. Dotted horizontal lines extending outside the boxes represent the total (black, left column) and maximum daily (red, right column) ERA5 precipitation values for the validation years 2018-2019.

6. Discussion and Conclusions

We proposed the KCDE approach for estimating the CDF of skewed probability distributions with emphasis on precipitation amount. KCDE is based on non-parametric estimates of the CDF which are obtained by means of explicit integration of underlying kernel functions. We showed that KCDE equipped with the BGK plug-in bandwidth [44] estimates skewed probability distributions more accurately than the empirical staircase estimator or KDE with the normal reference rule (Section 3 and Appendix C). These results suggest that the BGK bandwidth, which is based on rigorous statistical theory, can efficiently adapt to the shape of the probability distribution. To our knowledge this is the first application of the BGK bandwidth in non-parametric precipitation analysis. As shown in Section 3.2 the BGK bandwidth used with compactly supported kernels in several cases out-performs the Gaussian kernel when estimating the CDF of skewed probability distributions.

Our analysis focused on synthetic data from parametric probability distributions and ERA5 reanalysis data. We did not include observation data in this study because the available record for Crete is very sparse, with a large fraction of missing values [46]. In the reanalysis data sets we assumed non-zero precipitation amounts, hence we focused on the wet season. We replaced zero amounts with small finite numbers (randomly distributed between the floating point relative accuracy of the machine and the minimum non-zero amount in the respective data set). Hence, we did not attempt to model the occurrence of precipitation. This can be achieved with Markov chain methods [69], or by means of censored latent Gaussian processes [70, 71].

Taking advantage of the explicit equations for the CDF kernel steps, we formulated an ITS simulation method based on KCDE which is suitable for non-Gaussian distributions. In its current form, the ITS simulation method does not account for correlations between precipitation amounts at different times. Precipitation data, however, exhibit short-range correlations (e.g., over a couple of days for the daily amounts) as evidenced in the variogram function (not shown herein). Such dependence can be introduced in the simulations *a posteriori*: A Monte Carlo approach can be used in which simulated values are shuffled aiming to optimize a correlation cost functional. This procedure is computationally expensive and also unnecessary for estimating total precipitation amounts over a given period of time as shown in Section 5. Regarding the use of simulations to design protective measures

against extreme precipitation, our investigations show the 95% percentile of maximum daily precipitation predicted by ITS based on 1000 simulated states provides an adequate estimate for most years.

In general, it is accepted in non-parametric estimation that no single kernel function or bandwidth estimate is optimal in every case. We have found that the BGK bandwidth has advantages for the probability models studied. However, this finding cannot be generalized to all possible distribution functions. Thus, more research is needed to further investigate the conditions under which the BGK bandwidth is optimal. Finally, to successfully apply KCDE for simulation purposes, training data over a long observation window are needed, in order to capture rare events. This is exemplified by the unsatisfactory performance of the simulation for the year 2019 as discussed in Section 5. The issue of adequate sample size is all the more pertinent in light of climate change.

Finally, our analysis focused on precipitation modeling for the Mediterranean island of Crete. However, the proposed KCDE method for non-parametric estimation of probability distributions and the associated ITS simulation method can be applied to study precipitation amount in different geographical areas and climates.

Acknowledgments

This research is co-financed by Greece and the European Union (European Social Fund- ESF) through the Operational Programme «Human Resources Development, Education and Lifelong Learning 2014-2020» in the context of the project “Gaussian Anamorphosis with Kernel Estimators for Spatially Distributed Data and Time Series and Applications in the Analysis of Precipitation” (MIS 5052133).

References

- [1] Z. Li, F. Brissette, J. Chen, Finding the most appropriate precipitation probability distribution for stochastic weather generation and hydrological modelling in nordic watersheds, *Hydrological Processes* 27 (25) (2013) 3718–3729. doi:10.1002/hyp.9499.
- [2] L. Ye, L. S. Hanson, P. Ding, D. Wang, R. M. Vogel, The probability distribution of daily precipitation at the point and catchment scales in the United States, *Hydrology and Earth System Sciences* 22 (12) (2018) 6519–6531. doi:10.5194/hess-22-6519-2018.
- [3] H.-K. Cho, K. P. Bowman, G. R. North, A comparison of gamma and lognormal distributions for characterizing satellite rain rates from the tropical rainfall measuring mission, *Journal of Applied Meteorology* 43 (11) (2004) 1586–1597. doi:10.1175/JAM2165.1.
- [4] D. S. Wilks, Maximum likelihood estimation for the gamma distribution using data containing zeros, *Journal of Climate* 3 (12) (1990) 1495–1501. doi:10.1175/1520-0442(1990)003<1495:MLEFTG>2.0.CO;2.
- [5] D. S. Wilks, K. L. Eggleston, Estimating monthly and seasonal precipitation distributions using the 30-and 90-day outlooks, *Journal of Climate* 5 (3) (1992) 252–259. doi:10.1175/1520-0442(1992)005<0252:EMASPD>2.0.CO;2.
- [6] N. T. Ison, A. M. Feyerherm, L. D. Bark, Wet period precipitation and the gamma distribution, *Journal of Applied Meteorology and Climatology* 10 (4) (1971) 658–665. doi:10.1175/1520-0450(1971)010<0658:WPPATG>2.0.CO;2.
- [7] R. Biondini, Cloud motion and rainfall statistics, *Journal of Applied Meteorology and Climatology* 15 (3) (1976) 205–224. doi:10.1175/1520-0450(1976)015<0205:CMARS>2.0.CO;2.
- [8] B. Kedem, L. S. Chiu, On the lognormality of rain rate, *Proceedings of the National Academy of Sciences* 84 (4) (1987) 901–905. doi:10.1073/pnas.84.4.901.

- [9] H. Sauvageot, The probability density function of rain rate and the estimation of rainfall by area integrals, *Journal of Applied Meteorology and Climatology* 33 (11) (1994) 1255 – 1262. doi:10.1175/1520-0450(1994)033<1255:TPDFOR>2.0.CO;2.
- [10] R. E. López, The lognormal distribution and cumulus cloud populations, *Monthly Weather Review* 105 (7) (1977) 865 – 872. doi:10.1175/1520-0493(1977)105<0865:TLDACC>2.0.CO;2.
- [11] T. Shoji, H. Kitaura, Statistical and geostatistical analysis of rainfall in central Japan, *Computers & Geosciences* 32 (8) (2006) 1007–1024. doi:10.1016/j.cageo.2004.12.012.
- [12] D. A. Short, K. Nakamura, TRMM radar observations of shallow precipitation over the tropical oceans, *Journal of Climate* 13 (23) (2000) 4107–4124. doi:10.1175/1520-0442(2000)013<4107:TR00SP>2.0.CO;2.
- [13] J. Foster, M. Bevis, Lognormal distribution of precipitable water in Hawaii, *Geochemistry, Geophysics, Geosystems* 4 (7) (2003) 1065. doi:10.1029/2002GC000478.
- [14] J. Foster, M. Bevis, W. Raymond, Precipitable water and the lognormal distribution, *Journal of Geophysical Research: Atmospheres* 111 (D15). doi:10.1029/2005JD006731.
- [15] B. Kedem, L. S. Chiu, G. R. North, Estimation of mean rain rate: Application to satellite observations, *Journal of Geophysical Research: Atmospheres* 95 (D2) (1990) 1965–1972. doi:10.1029/JD095iD02p01965.
- [16] Z. Wang, Z. Zeng, C. Lai, W. Lin, X. Wu, X. Chen, A regional frequency analysis of precipitation extremes in mainland china with fuzzy c-means and L-moments approaches, *International Journal of Climatology* 37 (S1) (2017) 429–444. doi:10.1002/joc.5013.
- [17] S. Coles, *An introduction to statistical modeling of extreme values*, Springer Series in Statistics, Springer-Verlag, London, 2001.
- [18] D. Gellens, Combining regional approach and data extension procedure for assessing GEV distribution of extreme precipitation in Belgium, *Journal of Hydrology* 268 (1-4) (2002) 113–126. doi:10.1016/S0022-1694(02)00160-9.

- [19] M. Scheuerer, Probabilistic quantitative precipitation forecasting using Ensemble Model Output Statistics, *Quarterly Journal of the Royal Meteorological Society* 140 (680) (2014) 1086–1096. doi:10.1002/qj.2183.
- [20] D. Koutsoyiannis, Statistics of extremes and estimation of extreme rainfall: II. empirical investigation of long rainfall records, *Hydrological Sciences Journal* 49 (4) (2004) 591–610. doi:10.1623/hysj.49.4.591.54424.
- [21] A. Schindler, D. Maraun, J. Luterbacher, Validation of the present day annual cycle in heavy precipitation over the British islands simulated by 14 RCMs, *Journal of Geophysical Research: Atmospheres* 117 (2012) D18107. doi:10.1029/2012JD017828.
- [22] V. V. Kharin, F. W. Zwiers, X. Zhang, G. C. Hegerl, Changes in temperature and precipitation extremes in the IPCC ensemble of global coupled model simulations, *Journal of Climate* 20 (8) (2007) 1419–1444. doi:10.1175/JCLI4066.1.
- [23] S. M. Papalexiou, D. Koutsoyiannis, Entropy based derivation of probability distributions: A case study to daily rainfall, *Advances in Water Resources* 45 (2012) 51–57. doi:10.1016/j.advwatres.2011.11.007.
- [24] H. Rho, J. H. Kim, Modelling the entire range of daily precipitation using phase-type distributions, *Advances in Water Resources* 123 (2019) 210–224. doi:10.1016/j.advwatres.2018.11.014.
- [25] R. A. Fisher, L. H. C. Tippett, Limiting forms of the frequency distribution of the largest or smallest member of a sample, *Mathematical Proceedings of the Cambridge Philosophical Society* 24 (2) (1928) 180–190. doi:10.1017/S0305004100015681.
- [26] B. Gnedenko, Sur la distribution limite du terme maximum d’une serie aleatoire, *Annals of Mathematics* 44 (3) (1943) 423–453. doi:10.2307/1968974.
- [27] C. Martinez-Villalobos, J. D. Neelin, Why do precipitation intensities tend to follow gamma distributions?, *Journal of the Atmospheric Sciences* 76 (11) (2019) 3611–3631. doi:10.1175/JAS-D-18-0343.1.

- [28] O. Vlček, R. Huth, Is daily precipitation gamma-distributed?: Adverse effects of an incorrect use of the Kolmogorov–Smirnov test, *Atmospheric Research* 93 (4) (2009) 759–766. doi:10.1016/j.atmosres.2009.03.005.
- [29] V. Agou, Geostatistical analysis of precipitation on the island of Crete, Master’s thesis, Technical University of Crete, Chania, Crete, 73100 Greece (2016). doi:10.26233/heallink.tuc.62773.
- [30] Anonymous, The state of the global climate 2020, World Meteorological Organization: Available online: https://library.wmo.int/doc_num.php?explnum_id=10618, accessed on August 3, 2021 (2021).
- [31] H. Madsen, D. Lawrence, M. Lang, M. Martinkova, T. Kjeldsen, Review of trend analysis and climate change projections of extreme precipitation and floods in Europe, *Journal of Hydrology* 519 (2014) 3634–3650. doi:10.1016/j.jhydrol.2014.11.003.
- [32] C. Martinez-Villalobos, J. D. Neelin, Climate models capture key features of extreme precipitation probabilities across regions, *Environmental Research Letters* 16 (2) (2021) 024017. doi:10.1088/1748-9326/abd351.
- [33] M. Rosenblatt, Remarks on some nonparametric estimates of a density function, *The Annals of Mathematical Statistics* 27 (3) (1956) 832–837. doi:10.1214/aoms/1177728190.
- [34] E. Parzen, On estimation of a probability density function and mode, *The Annals of Mathematical Statistics* 33 (3) (1962) 1065–1076. doi:10.1214/aoms/1177704472.
- [35] S. Ghosh, *Kernel Smoothing: Principles, Methods and Applications*, John Wiley & Sons, Hoboken, NJ, USA, 2018.
- [36] B. U. Park, J. S. Marron, Comparison of data-driven bandwidth selectors, *Journal of the American Statistical Association* 85 (409) (1990) 66–72. doi:10.1080/01621459.1990.10475307.
- [37] M. P. Wand, M. C. Jones, *Kernel Smoothing*, Monographs on Statistics & Applied Probability, CRC Press, 1994.

- [38] M. C. Jones, J. S. Marron, S. J. Sheather, A brief survey of bandwidth selection for density estimation, *Journal of the American Statistical Association* 91 (433) (1996) 401–407. doi:10.2307/2291420.
- [39] S. J. Sheather, M. C. Jones, A reliable data-based bandwidth selection method for kernel density estimation, *Journal of the Royal Statistical Society: Series B (Methodological)* 53 (3) (1991) 683–690. doi:10.2307/2345597.
- [40] D. W. Scott, *Multivariate Density Estimation: Theory, Practice, and Visualization*, John Wiley & Sons, 2015.
- [41] A. Sharma, U. Lall, A nonparametric approach for daily rainfall simulation, *Mathematics and Computers in Simulation* 48 (4) (1999) 361–371. doi:10.1016/S0378-4754(99)00016-6.
- [42] T. I. Harrold, A. Sharma, S. J. Sheather, A nonparametric model for stochastic generation of daily rainfall amounts, *Water Resources Research* 39 (12). doi:10.1029/2003WR002570.
- [43] T. Mosthaf, A. Bárdossy, Regionalizing nonparametric models of precipitation amounts on different temporal scales, *Hydrology and Earth System Sciences* 21 (5) (2017) 2463–2481. doi:/10.5194/hess-21-2463-2017.
- [44] Z. I. Botev, J. F. Grotowski, D. Kroese, Kernel density estimation via diffusion, *The Annals of Statistics* 38 (5) (2010) 2916–2957. doi:10.1214/10-AOS799.
- [45] E. A. Varouchakis, G. A. Corzo, G. P. Karatzas, A. Kotsopoulou, Spatio-temporal analysis of annual rainfall in Crete, Greece, *Acta Geophysica* 66 (3) (2018) 319–328. doi:10.1007/s11600-018-0128-z.
- [46] V. D. Agou, E. A. Varouchakis, D. T. Hristopulos, Geostatistical analysis of precipitation in the island of Crete (Greece) based on a sparse monitoring network, *Environmental Monitoring and Assessment* 191 (353) (2019) 1573–2959. doi:10.1007/s10661-019-7462-8.
- [47] S. D. Nerantzaki, D. T. Hristopulos, N. P. Nikolaidis, Estimation of the uncertainty of hydrologic predictions in a karstic Mediterranean watershed, *Science of The Total Environment* 717 (2020) 137131. doi:10.1016/j.scitotenv.2020.137131.

- [48] A. Papoulis, S. U. Pillai, Probability, Random Variables and Stochastic Processes, 4th Edition, McGraw Hill, New York, NY, 2002.
- [49] D. T. Hristopulos, Random Fields for Spatial Data Modeling: A Primer for Scientists and Engineers, Springer/Nature, Dordrecht, the Netherlands, 2020. doi:10.1007/978-94-024-1918-4.
- [50] L. de Haan, A. Ferreira, Extreme Value Theory: An Introduction (Springer Series in Operations Research and Financial Engineering), 1st Edition, Springer, New York, NY 10013, U.S.A., 2010. doi:10.1007/0-387-34471-3.
- [51] M. Abramowitz, I. A. Stegun, R. H. Romer, Handbook of Mathematical Functions with Formulas, Graphs, and Mathematical Tables, American Association of Physics Teachers, 1988.
- [52] Y.-C. Chen, A tutorial on kernel density estimation and recent advances, *Biostatistics & Epidemiology* 1 (1) (2017) 161–187. doi:10.1080/24709360.2017.1396742.
- [53] C.-Y. Chu, D. J. Henderson, C. F. Parmeter, Plug-in bandwidth selection for kernel density estimation with discrete data, *Econometrics* 3 (2) (2015) 199–214. doi:10.3390/econometrics3020199.
- [54] D. A. Benson, D. Bolster, S. Pankavich, M. J. Schmidt, Nonparametric, data-based kernel interpolation for particle-tracking simulations and kernel density estimation, *Advances in Water Resources* 152 (2021) 103889. doi:10.1016/j.advwatres.2021.103889.
- [55] M. C. Jones, Simple boundary correction for kernel density estimation, *Statistics and Computing* 3 (3) (1993) 135–146. doi:10.1007/BF00147776.
- [56] P. Malec, M. Schienle, Nonparametric kernel density estimation near the boundary, *Computational Statistics & Data Analysis* 72 (2014) 57–76. doi:10.1007/978-3-319-71688-6.
- [57] Y. Xiao, H. Wang, L. Zhang, W. Xu, Two methods of selecting Gaussian kernel parameters for one-class SVM and their application to fault detection, *Knowledge-Based Systems* 59 (2014) 75–84. doi:10.1016/j.knosys.2014.01.020.

- [58] S. Kitayama, K. Yamazaki, Simple estimate of the width in Gaussian kernel with adaptive scaling technique, *Applied Soft Computing* 11 (8) (2011) 4726–4737. doi:10.1016/j.asoc.2011.07.011.
- [59] G. Kusano, Y. Hiraoka, K. Fukumizu, Persistence weighted Gaussian kernel for topological data analysis, in: M. F. Balcan, K. Q. Weinberger (Eds.), *Proceedings of The 33rd International Conference on Machine Learning*, Vol. 48 of *Proceedings of Machine Learning Research*, New York, NY, USA, 2016, pp. 2004–2013.
- [60] B. W. Silverman, *Density Estimation for Statistics and Data Analysis* (Monographs on Statistics and Applied Probability, Band 26) , Chapman and Hall, London, UK, 1986.
- [61] S. J. Sheather, *Density Estimation*, *Statistical Science* 19 (4) (2004) 588 – 597. doi:10.1214/088342304000000297.
- [62] Copernicus Climate Change Service C3S, ERA5: Fifth generation of ECMWF atmospheric reanalyses of the global climate, data retrieved from: <https://cds.climate.copernicus.eu/cdsapp#!/home> (2018).
- [63] P. T. Nastos, C. S. Zerefos, Spatial and temporal variability of consecutive dry and wet days in Greece, *Atmospheric Research* 94 (4) (2009) 616–628. doi:10.1016/j.atmosres.2009.03.009.
- [64] X. L. Wang, H. Chen, Y. Wu, Y. Feng, Q. Pu, New techniques for the detection and adjustment of shifts in daily precipitation data series, *Journal of Applied Meteorology and Climatology* 49 (12) (2010) 2416 – 2436. doi:10.1175/2010JAMC2376.1.
- [65] G. Tang, Characterization of the systematic and random errors in satellite precipitation using the multiplicative error model, *IEEE Transactions on Geoscience and Remote Sensing* 59 (7) (2021) 5407–5416. doi:10.1109/TGRS.2020.3028525.
- [66] Google Earth, Crete island, Greece, SIO, NOAA, U.S. Navy, NGA, GEBCO. DigitalGlobe 2015. Data retrieved from: <http://www.earth.google.com> (2015).

- [67] E. A. Varouchakis, D. T. Hristopulos, Improvement of groundwater level prediction in sparsely gauged basins using physical laws and local geographic features as auxiliary variables, *Advances in Water Resources* 52 (2013) 34–49. doi:10.1016/j.advwatres.2012.08.002.
- [68] A. Mamara, E. Chatziapostolou, N. Karatarakis, Annual bulletin on the climate in Greece 2019, Report, Hellenic National Meteorological Service, [Last accessed 6 September 2021 from http://www.hnms.gr/emy/el/pdf/2019_GRsignificantEVENT_gr.pdf] (2019).
- [69] T. I. Harrold, A. Sharma, S. J. Sheather, A nonparametric model for stochastic generation of daily rainfall occurrence, *Water Resources Research* 39 (10) (2003) 1300. doi:10.1029/2003WR002182.
- [70] A. Baxevani, J. Lennatsson, A spatiotemporal precipitation generator based on a censored latent Gaussian field, *Water Resources Research* 51 (6) (2015) 4338–4358. doi:10.1002/2014WR016455.
- [71] D. Allard, M. Bourotte, Disaggregating daily precipitations into hourly values with a transformed censored latent Gaussian process, *Stochastic Environmental Research and Risk Assessment* 29 (2) (2015) 453–462. doi:10.1007/s00477-014-0913-4.

Appendix A. Integrals for CDF kernel steps

The change of variables $(z - z_{[i]})/h \rightarrow u_i$ implies $dz = h du_i$. Then, the CDF kernel step defined by Eq. (5) is expressed as

$$\tilde{K}(u_i) = \int_{-\infty}^{u_i} du' K(u'). \quad (\text{A.1})$$

Compact kernels are of the general form $K(u) = g(u) \mathbb{I}(|u| \leq 1)$, where $\mathbb{I}(|u| \leq 1)$ is the indicator function: $\mathbb{I}(|u| \leq 1) = 1$ if $|u| \leq 1$ and $\mathbb{I}(|u| \leq 1) = 0$ otherwise. For compact kernels, Eq. (A.1) is expressed as follows

$$\tilde{K}(u_i) = \mathbb{I}(u_i > -1) \int_{-1}^{\tilde{u}_i} du' g(u'), \quad (\text{A.2})$$

where $\tilde{u}_i = \min(1, u_i)$. The above implies that the CDF kernel step vanishes if $u_i < -1$ for compact kernels. This reflects the fact that the sample value $z_{[i]}$ does not contribute to the CDF at z , since the latter is more than one bandwidth less than $z_{[i]}$. Below we explicitly calculate the integrals (A.2) for the quadratic and Epanechnikov kernels. The CDF steps for other kernels are similarly calculated (see also Table 1).

Appendix A.1. Quadratic kernel

The quadratic kernel is defined by means of the equation

$$K(u) = \frac{3}{4}(1 - u^2) \mathbb{I}(|u| \leq 1). \quad (\text{A.3})$$

Thus, the CDF kernel step for $u_i > -1$ is given by

$$\begin{aligned} \tilde{K}(u_i) &= \frac{3}{4} \int_{-1}^{\tilde{u}_i} du (1 - u)^2 = \frac{3}{4} \left[u - \frac{u^3}{3} \right]_{-1}^{\tilde{u}_i} \\ &= \frac{3}{4} \left(\tilde{u}_i - \frac{1}{3} \tilde{u}_i^3 + \frac{2}{3} \right). \end{aligned} \quad (\text{A.4})$$

Appendix A.2. Epanechnikov kernel

The Epanechnikov kernel is defined by means of the equation,

$$K(u) = \frac{3}{2}(1 - |u|)^2 \mathbb{I}_{|u| \leq 1}(u). \quad (\text{A.5})$$

Thus, the CDF kernel step for $u_i > -1$ is given by

$$\begin{aligned}\tilde{K}(u_i) &= \frac{3}{2} \int_{-1}^{\tilde{u}_i} du (1 - |u|)^2 = \frac{3}{2} \left[\frac{u_i^3}{3} - u_i |u_i| + u_i \right]_{-1}^{\tilde{u}_i} \\ &= \frac{3}{2} \left[\frac{\tilde{u}_i^3}{3} - \tilde{u}_i^2 \operatorname{sgn}(u_i) + \tilde{u}_i + \frac{1}{3} \right].\end{aligned}\tag{A.6}$$

Appendix B. BGK Bandwidth Estimation

This appendix reviews the details of BGK bandwidth estimation. The estimate employs an auxiliary bandwidth \hat{a}_1 , which is obtained from a sequence of bandwidths $a_{j;n}$, $j = l, l-1, \dots, 1$. The index $n = 0, 1, \dots, n^*$ counts the number of repetitions until convergence is achieved, while l is a pre-selected recursion depth (usually $l = 7$).

The sequence is initialized by arbitrarily setting $a_{l+1;0}$ equal to the machine precision; the $a_{j;n}$ for given n are generated by means of the following recursive expression

$$a_{j;n}^2 = \left(\frac{1 + 2^{-(j+1/2)}}{3} \frac{1 \times 3 \cdots \times (2j-1)}{N \sqrt{\pi/2} G[\hat{f}_n^{(j+1)}(z)]} \right)^{2/(2j+3)}, \quad j = l, l-1, \dots, 1.\tag{B.1}$$

In the above, $G[\hat{f}_n^{(j+1)}(\cdot)]$ is defined in Eq. (7), and $\hat{f}_n^{(j+1)}(\cdot)$ is the kernel-based PDF estimate with bandwidth $a_{j+1;n}$; the latter requires recursive calculation of $\hat{f}_n^{(j+2)}(\cdot)$. If $a_{j=l;n}$ is known, then $G[\hat{f}_n^{(l)}(z)]$ is also known, and $a_{j;n}$, $l > j \geq 1$ follow by iterative application of Eq. (B.1) for progressively smaller j .

For $n = 0$ it is assumed that the initial bandwidth $a_{l;0}$ can be estimated using as $\hat{f}_n^{(l+1)}(\cdot)$ in Eq. (B.1) a Gaussian PDF with mean and variance estimated from the data. One could then estimate the auxiliary bandwidth from Eq. (B.1) for $n = 0$ without further repetition. However, as shown in [44], if the true distribution deviates significantly from the normal, suboptimal estimates of h are then obtained from this initial condition. Better results are obtained by progressively refining the auxiliary bandwidth estimates.

For $n \geq 1$ we initialize Eq. (B.1) using as initial PDF (for $j = l$) the KDE estimate with bandwidth $a_{1;n-1}$, i.e., the PDF $\hat{f}_{n-1}^{(1)}(\cdot)$ from the previous stage. The repetition count increases up to n^* such that $|a_{1;n^*} - a_{1;n^*-1}| < \epsilon$ is obtained for the first time. Then we set $\hat{a}_1 = a_{1;n^*}$. From Eq. (7) and \hat{a}_1 the BGK bandwidth h is calculated.

Appendix C. KCDE with Normal Reference Bandwidth

This appendix presents boxplots of the mean square error ratios that compare the performance of the kernel Density Estimator using the normal reference rule for bandwidth selection (see Section 3.1). The figures illustrate that the normal reference rule doesn't provide a CDF that significantly improves the estimation compared to the staircase function.

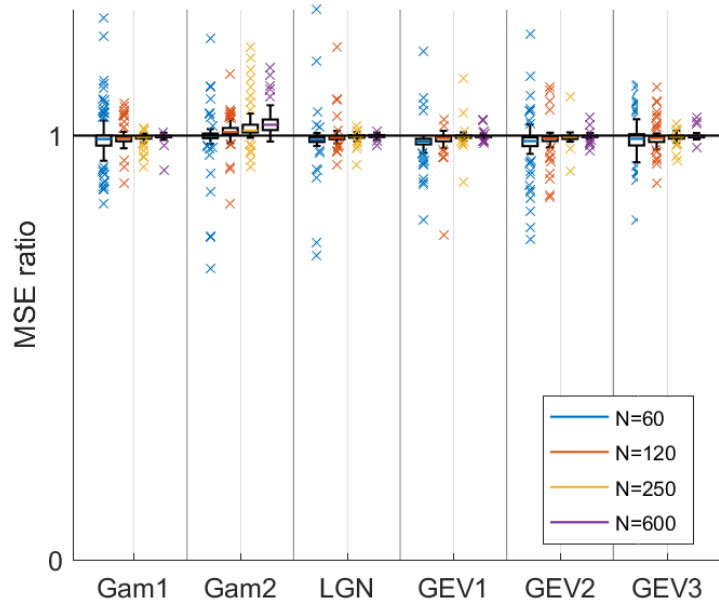


Figure C1: Boxplots of the ratio between the MSE of the CDF \hat{F}_K with the normal reference rule as bandwidth (for the Spherical kernel) and the theoretical CDF F divided by the MSE between the staircase function estimate \hat{F}_s and the CDF F . N is the sample size ($N = 60, 120, 250, 600$). The abbreviations of the probability models (Gam1, Gam2, LGN, GEV1, GEV2, GEV3) are defined in the main text.

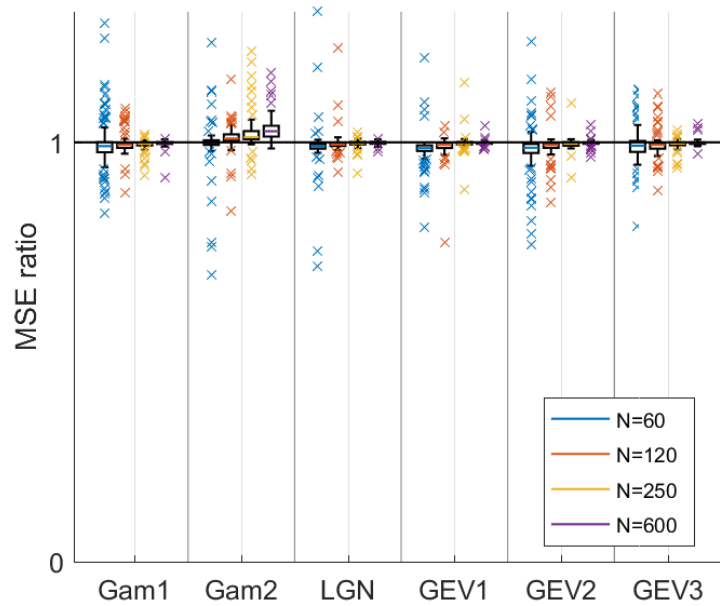


Figure C2: Boxplots of the ratio between the MSE of the CDF \hat{F}_K with the normal reference rule as bandwidth (for the triweight kernel) and the theoretical CDF F divided by the MSE between the staircase function estimate \hat{F}_s and the CDF F . N is the sample size ($N = 60, 120, 250, 600$). The abbreviations of the probability models (Gam1, Gam2, LGN, GEV1, GEV2, GEV3) are defined in the main text.

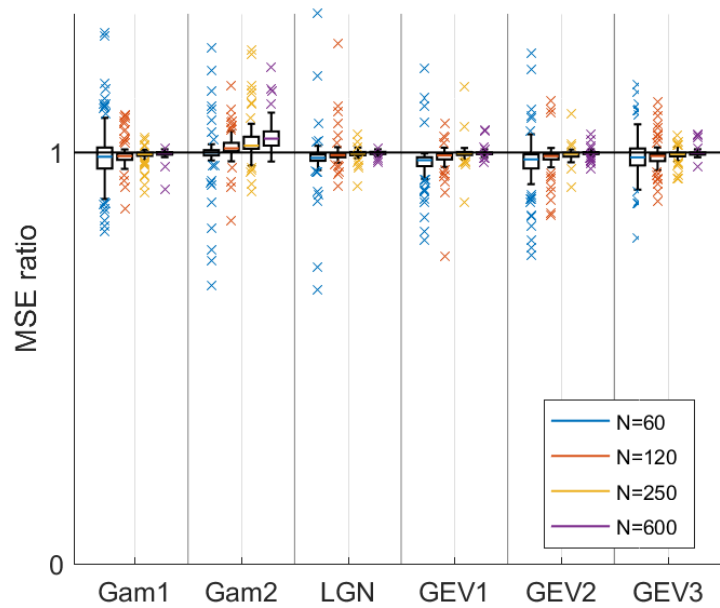


Figure C3: Boxplots of the ratio between the MSE of the CDF \hat{F}_K with the normal reference rule as bandwidth (for the Quadratic kernel) and the theoretical CDF F divided by the MSE between the staircase function estimate \hat{F}_s and the CDF F . N is the sample size ($N = 60, 120, 250, 600$). The abbreviations of the probability models (Gam1, Gam2, LGN, GEV1, GEV2, GEV3) are defined in the main text.

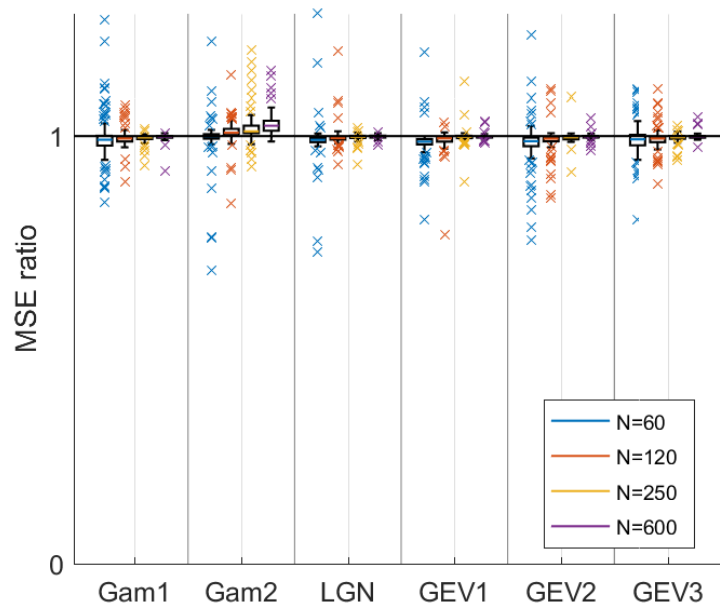


Figure C4: Boxplots of the ratio between the MSE of the CDF \hat{F}_K with the normal reference rule as bandwidth (for the Epanechnikov kernel) and the theoretical CDF F divided by the MSE between the staircase function estimate \hat{F}_s and the CDF F . N is the sample size ($N = 60, 120, 250, 600$). The abbreviations of the probability models (Gam1, Gam2, LGN, GEV1, GEV2, GEV3) are defined in the main text.

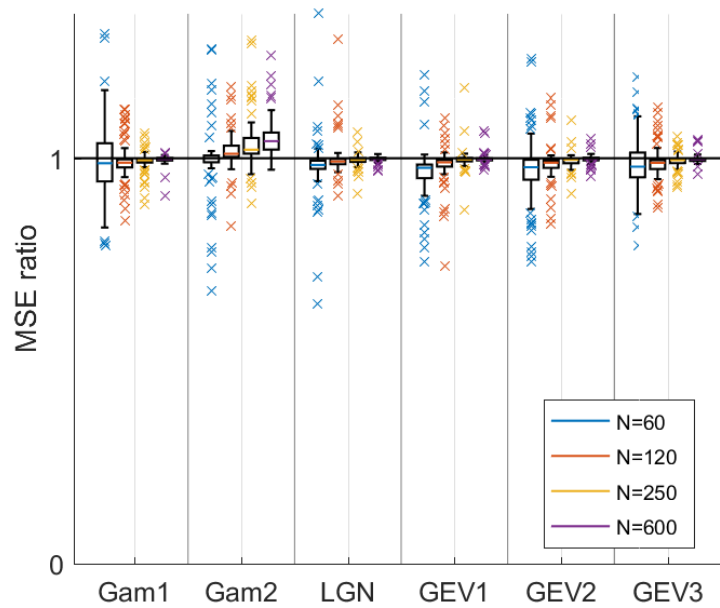


Figure C5: Boxplots of the ratio between the MSE of the CDF \hat{F}_K with the normal reference rule as bandwidth (for the Uniform kernel) and the theoretical CDF F divided by the MSE between the staircase function estimate \hat{F}_s and the CDF F . N is the sample size ($N = 60, 120, 250, 600$). The abbreviations of the probability models (Gam1, Gam2, LGN, GEV1, GEV2, GEV3) are defined in the main text.